Galvanic coupling between AA7075-T6 and AA2024-T3 intensifies local corrosion

Mopon, Marlon; Mol, Arjan; Garcia, Santiago J.

DOI
10.1016/j.electacta.2025.147335

Publication date
2025

Document Version
Final published version

Published in
Electrochimica Acta

Citation (APA)
Mopon, M., Mol, A., & Garcia, S. J. (2025). Galvanic coupling between AA7075-T6 and AA2024-T3 intensifies local corrosion. *Electrochimica Acta*, *541*, Article 147335.
https://doi.org/10.1016/j.electacta.2025.147335

Electrochimica Acta 541 (2025) 147335

Contents lists available at ScienceDirect

Electrochimica Acta

journal homepage: www.journals.elsevier.com/electrochimica-acta

Galvanic coupling between AA7075-T6 and AA2024-T3 intensifies local corrosion

Marlon Mopon Jr. [a,b,*], Arjan Mol [c], Santiago J. Garcia [a,**]

[a] Aerospace Structures and Materials Department, Delft University of Technology, Delft, the Netherlands
[b] Department of Chemical Engineering, University of the Philippines Diliman, Quezon City, Philippines
[c] Department of Materials Science and Engineering, Delft University of Technology, Delft, the Netherlands

ARTICLE INFO

Keywords:
Galvanic corrosion
Localized corrosion
In situ analysis
Galvanic potential
Galvanic current

ABSTRACT

This study demonstrates that galvanically coupling AA2024-T3 and AA7075-T6 affects localized corrosion even with the alloys' comparable electrochemical behaviour. In situ reflected light microscopy tracked corrosion initiation and trench propagation, while zero resistance ammeter measurements quantified galvanic current density and potential. This combined approach allowed direct correlation between electrochemical signals and optically detectable surface phenomena. Galvanic coupling increased cathodic activity at AA2024-T3 intermetallic particles (IMPs) and caused the surrounding matrix to dissolve more extensively beyond the trench that formed around the particles. Local activity analysis revealed initial IMP dealloying was unaffected by galvanic coupling. However, lateral growth of trenches in both alloys was accelerated under coupling compared with electrically-isolated conditions. Correlation of optical activity with electrochemical measurements showed that trends and fluctuations in galvanic current and potential reflect different stages of local corrosion, facilitating the morphological and physicochemical interpretation of the electrochemical data.

1. Introduction

Aluminium alloys AA2024 (Al-Cu-Mg) and AA7075 (Al-Zn-Mg-Cu) are widely used in aerospace and automotive applications due to their high strength-to-weight ratios and favourable mechanical performance. Despite these advantages, both alloys are susceptible to corrosion, particularly in chloride-containing environments due to the presence of intermetallic particles (IMPs) formed during manufacturing and thermomechanical processing [1–5]. In AA2024, localized corrosion initiates with particle dealloying followed by dissolution of the surrounding matrix (i.e., trenching) once microgalvanic coupling is established [6–8]. This sequence of events is observed across IMP compositions, though S-phase (Al_2CuMg) particles corrode fastest [8] and reportedly account for the majority of local corrosion events [9]. Other IMPs present in AA2024 include θ-phases (Al_2Cu) and Fe-containing particles. AA7075 shows similar local corrosion behaviour albeit with slight differences in the composition of IMPs involved. It also contains the active S-phases due to its Cu and Mg content, as well as Fe-containing particles (e.g., $Al_7Fe_2Cu(Mn)$, $Al_{15}(FeMn)_3(SiCu)_2$, Al_7Cu_2Fe), which are less active but still dealloy to varying degrees and can cause trenching [10–12]. Apart from local corrosion around IMPs, AA7075 is also prone to the rapid dissolution of an altered surface layer [13,14]. The dissolution of this surface layer leads to rapidly propagating corrosion streaks, earning it the name streaking corrosion [15–17]. In a recent work [15], we have shown that streaking corrosion preferentially initiates at intermetallics and is also characterized by a distinct sequence of transients when concurrent open-circuit potential (OCP) measurements are performed.

In practical applications, AA2024 and AA7075 are often joined with other metals or alloys. The presence of electrical contact and a bridging electrolyte to complete the circuit can lead to the creation of galvanic couples between the aluminium alloys and the other materials which can further complicate and potentially aggravate their corrosion behaviour. Common pairings, such as AA2024 or AA7075 with steel [18–25], titanium [25–29], or carbon fibre composites [30–33], have been extensively studied due to their widespread use in multi-material assemblies. In these combinations, the aluminium alloys represent the less noble component and therefore corrode preferentially. Although AA2024 and AA7075 are both aluminium-based, galvanic coupling can also occur between them due to differences in their alloying elements -

---

[*] Corresponding author at: Aerospace Structures and Materials Department, Delft University of Technology, Delft, the Netherlands.
[**] Corresponding author.

E-mail addresses: m.mopon@tudelft.nl (M. Mopon), s.j.garciaespallargas@tudelft.nl (S.J. Garcia).

https://doi.org/10.1016/j.electacta.2025.147335
Received 29 July 2025; Received in revised form 29 August 2025; Accepted 6 September 2025

primarily copper in AA2024 and zinc in AA7075. Such coupling, while less common, is relevant in structural configurations where both alloys are in electrical contact, such as in the skin-stiffener assemblies of aircraft [34,35]. Notably, corrosion studies on this specific AA2024–AA7075 configuration focused primarily on the local corrosion behaviour arising from the microstructural zones created by friction-stir welding of the two alloys [36–39]. Using a similar system comprised of AA2024 and AA7475 (i.e., an AA7XXX alloy with lower amounts of Fe and Si, and lower IMP density), Bugarin et al. [40] reported low impedances at the stir zone of the welded alloys due to the galvanic coupling of their thermomechanically affected zones (TMAZ), with the AA2024 TMAZ acting as the cathode and AA7475 as the anode. They noted though that the impedance values of the stir zone are closer to that of AA2024 TMAZ which they attributed to its higher concentration of precipitate particles rendering higher electrochemical activity. Local studies by de Abreu et al. [41] on friction-stir welded AA2024-AA7475 also showed that galvanic coupling of the system might lead to selective dissolution of Zn. The dissolved Zn can then redeposit on the surface of Al-Cu-Mg IMPs at prolonged exposure (∼24 h) to a corrosive environment. They also reported that the redeposition of Zn affected the dealloying behaviour of the Al-Cu-Mg IMPs. These findings highlight the interdependent relationship between localized corrosion at the IMP level and macroscale galvanic coupling. Interestingly, few studies analyse this interdependence even though corrosion of alloys like AA2024 and AA7075 have already been established to be highly local in nature. Furthermore, the few available studies mostly focus on welded configurations, which limits quantitative analysis of electrochemical interactions between the two alloys.

Other works that looked into the interplay between macroscale galvanic coupling and local corrosion mainly considered AA2024 coupled with more noble materials. Coelho et al. [28] showed that galvanic coupling between AA2024-T3 and Ti6Al4V of equal areas only led to faster disruption of the AA2024 passive layer, but not to any substantial dissolution. They attributed the absence of effective galvanic coupling to higher oxygen reduction reaction kinetics on AA2024, particularly on the Cu-rich sites, than that on the Ti alloy. Another work by Coelho et al. [42] on galvanically-coupled graphite and AA2024-T3 demonstrated that galvanic coupling behaviour is significantly dependent on the area ratio of the coupled materials. They reported that at an AA2024/graphite ratio of 10, only partial anodic polarization of the AA2024 surface is achieved. However, at an AA2024/graphite ratio of 1.5, complete anodic polarization of the AA2024 surface was observed through a combination of scanning vibrating electrode technique and scanning ion-selective electrode technique. They also reported minimal trenching around IMPs for this area ratio, potentially due to anodic polarization driving a relatively uniform dissolution of the alloy surface.

This work investigates how IMPs and their surrounding areas corrode when AA2024-T3 and AA7075-T6 are galvanically coupled in a chloride-rich aqueous environment. Unlike most material pairings studied in literature, these two alloys have comparable OCPs and are both prone to highly localized corrosion. Because of their electrochemical similarities, their coupling is considered a minor issue which leads to limited data on galvanic corrosion between them. Additionally, their tendency for localized attack makes it difficult to distinguish whether the observed corrosion is caused by galvanic coupling between the two alloys or simply by the usual microgalvanic interaction between IMPs and the matrix. Our recent works have shown that in situ reflected light microscopy can effectively reveal and quantify the kinetics of local degradation processes such as dealloying, trenching, oxide deposition, and streaking corrosion, with high spatial and temporal resolution [8,15,43,44]. Here, the technique is used to monitor local corrosion initiation and propagation at the surfaces of both alloys, capturing the morphological evolution of local attack. Simultaneously, in situ electrochemical measurements through a zero resistance ammeter (ZRA) provide a quantitative assessment of the galvanic interactions between the alloys during corrosion. By correlating visual and electrochemical data, this work aims to advance the mechanistic understanding of localized corrosion in galvanically-coupled dissimilar aluminium alloys.

2. Experimental

2.1. Materials

Commercial grade bare AA2024-T3 (Kaiser Aluminium, rolled thickness = 2 mm) and AA7075-T6 (Kaiser Aluminium, rolled thickness = 3 mm) were used for the corrosion tests. The metal sheets were used to prepare aluminium pillars (Fig. 1a) with exposed areas around 0.13 mm^2 as described elsewhere [8,43]. It is noted that the three sides of the pillar are specifically labelled (i.e., facing plane - FP, top plane - TP, bottom plane - BP) in the figure since they are relevant for positioning the pillars to form the assembly. A 0.05 M NaCl aqueous solution (>98 % purity NaCl in “Millipore Elix 3 UV” treated water) was used as the corrosive solution.

2.2. Sample preparation

The AA2024-T3 pillar was embedded in cold-curing epoxy through a previously established procedure described elsewhere [43]. Once fully cured, the epoxy was ground to expose side FP of the pillar. The unembedded AA7075-T6 pillar was then positioned next to the embedded AA2024-T3 pillar with the FP sides of both pillars facing each other. Insulating tape was placed between the two pillars to ensure the distance between them was minimized while at the same time preventing electrical contact. The separation distance for the pillars was ∼170 μm. The AA2024-AA7075 assembly was re-embedded in cold-curing epoxy to fix their positions (Fig. 1b). After complete curing, the top and bottom surfaces of the assembly were ground to expose the surfaces of the pillars. Electrical wire was connected to the BP side of each pillar to establish external electrical contact for in situ electrochemical measurements. Electrical separation between the pillars was confirmed with a multimeter. The bottom side of the assembly was embedded again in epoxy to maintain the placement of external connections and to avoid unwanted galvanic coupling between the copper contacts and the exposed surfaces of the aluminium pillars. After complete curing of the bottom side, side TA was ground to ensure that the top surfaces of the pillars are completely exposed. The final assembly had an AA2024 to AA7075 exposed area ratio close to 1.

2.3. In situ optical-electrochemical corrosion testing

The experimental protocol for immersion in the NaCl solution is similar to our previous work [8,43]. Prior to immersion, the sample surface was ground with SiC sandpaper from 320 to 4000 grit and then polished with 1 μm diamond paste. Pure ethanol was used for grinding and polishing. For immersion tests (Fig. 1c), the sample was placed in an electrochemical cell (redox.me Raman electrochemical flow cell) and mounted to a holder for in situ imaging during immersion with a reflected microscope (Dinolite AM7515MT4A, ca. 7–10 pixel μm^{-2}) operating in brightfield mode [43,45]. An Ivium CompactStat.h potentiostat was used to implement ZRA tests for the coupled alloys. The AA2024-T3 pillar was connected to the working electrode (WE) cable while the AA7075-T6 pillar was connected to the ground (GND) cable. The potential of the couple was measured against an Ag/AgCl(3 M KCl) reference electrode (RE) mounted to the electrochemical cell. In this configuration, a positive galvanic current corresponds to a net electron flow out of the working electrode (Supporting Information 1). Electrically-isolated (EI) tests wherein the alloys are separately corroding at their respective OCPs were also performed with the electrochemical cell. For these tests, the GND cable was connected to the earth ground while the WE cable is connected to the AA2024 or the AA7075 external electrical connection. The RE cable remains connected to the Ag/AgCl electrode. Once the assembly was mounted and

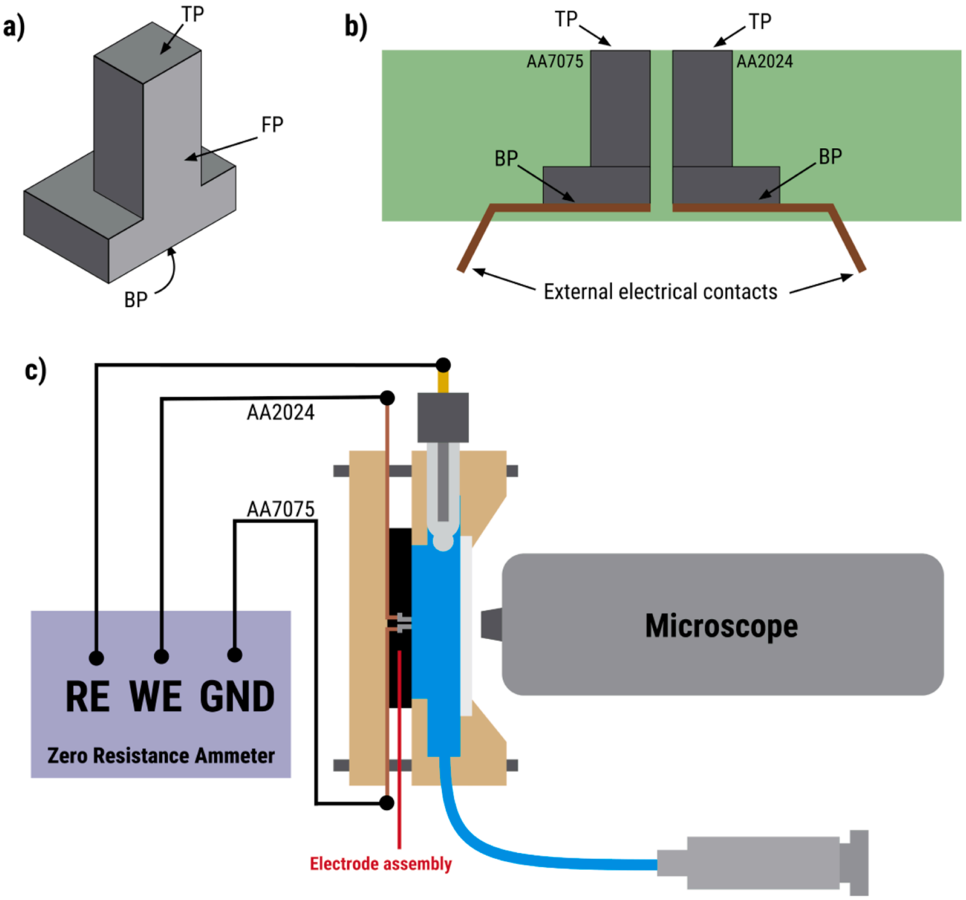

Fig. 1. Schematic of (a) an individual pillar with the labelled sides (top plane TP, bottom plane BP, facing plane FP), (b) the multi-pillar assembly embedded in epoxy, and (c) optical-electrochemical setup used for in situ analysis of assembly during immersion in corrosive electrolyte under galvanically-coupled conditions. During electrically-isolated tests, the ground (GND) cable is connected to the laboratory earth ground and the working electrode (WE) cable is connected to either the AA2024 or the AA7075 pillar.

recording started, a 5 mL volume of the electrolyte was injected into the cell using a syringe and monitoring proceeded for 2 h. Post-immersion analysis of the surfaces of the pillars was performed with scanning electron microscopy coupled with energy dispersive x-ray spectroscopy (SEM-EDX, JEOL JSM-7500F). Secondary electron images were acquired at a 15 kV accelerating voltage and a 10 μA emission current.

2.4. *Image analysis*

The image analysis protocol used for studying local changes in the sample surfaces is similar to our previous works [43,44]. Changes on both the AA2024 and AA7075 surfaces were quantified through image subtraction of the pre-processed (i.e., converted to grayscale, recursively realigned) microscopy images. It is noted that the images converted to grayscale each have an associated pixel gray-level. With the imaging conditions reported in Section 2.3 (i.e., brightfield imaging), local corrosion is observed as darkening of pixels. Image subtraction was performed with respect to the first image acquired during immersion (i.e., image at 0 s of immersion – image at x s of immersion) unless otherwise stated. The subtraction process quantifies the gray-level increase of a pixel at time t (i.e., activity level at time t). Its output is the global activity map (GAM) for the sample surface at time t. A built-in ImageJ look-up table (i.e., Fire) was used to colormap the GAMs for easier visualisation of the magnitude of the changes. The activity levels depicted in the GAMs range from 0 to 255, with 0 indicating no change with respect to the initial condition. Specific areas of the GAM were isolated for analysis of local surface changes (i.e., IMPs, trenches). This was achieved by overlaying boundaries manually extracted from active sites observed on the sample surface. It is noted that not all active sites present in the alloys were analysed. Sites with well-defined boundaries were prioritized for analysis. Supporting Information 2 shows the boundaries used for analysing changes on IMP surfaces and for assessing growth of trenches. The changes of the pixels within the defined boundaries were quantified and visualized through simplified pixel activity level distribution (sPAD) plots [43]. These plots present the maximum (maxAL), median (midAL), and minimum (minAL) activity levels as a function of time for the set of pixels on the IMP surface and reflect the intensity of the local changes.

3. Results and discussion

3.1. *Local corrosion progression of electrically-isolated AA2024 and AA7075*

Fig. 2a shows the corrosion behaviour of uncoupled AA2024 and AA7075 immersed in 0.05 M NaCl for two hours. Reflected light microscopy (RLM) images at 7200 s highlight the characteristic localized corrosion of both alloys consistent with previous studies [8,15,43]. As previously reported for AA2024 [8,43], its local corrosion features include visible dealloying of IMPs and trenching around them (see blue arrows in Fig. 2a – 7200 s). Corrosion product deposition (as indicated by cyan arrows in Fig. 2a – 7200 s) arising from cooperative corrosion of IMP clusters was also observed. Dealloying of IMPs, seen as darkening of their surfaces, is due to the dissolution of less noble components (e.g., Al, Mg) of the particles [6–8,43,44]. It is noted that the extent of dealloying is dependent on IMP composition. Particles with components that have a

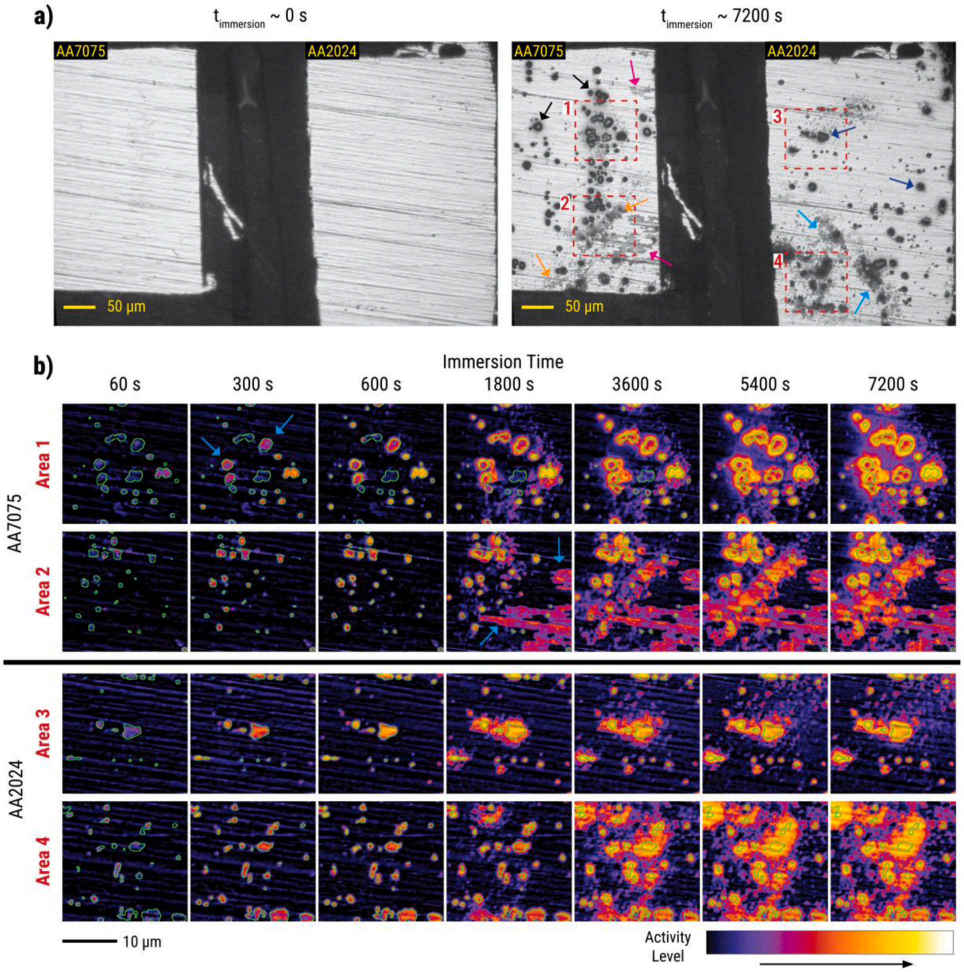

Fig. 2. Raw reflected microscopy images of the AA2024 and AA7075 samples (a) right before immersion and after 7200 s of immersion in 0.05 M NaCl. The alloys are not electrically connected and are corroding in electrically-isolated conditions. Evolution of local changes on the surfaces of the corroding alloys are shown in (b) activity maps of selected areas from the visible sections of the alloys. It is noted that the surface of the AA7075 is partially outside of the field of view of the microscope. The green boundaries indicate the boundaries used for analysing IMP activity.

significant difference in nobility (e.g., Cu vs. Al and Mg in S-phases) are more prone to extensive dealloying. Trenching, observed as dark circumferences around the particles, arises from microgalvanic coupling between the IMPs and the AA2024 matrix. Cathodic reactions on the IMP surface (e.g., oxygen reduction reaction) facilitate the anodic dissolution of the matrix [10,46]. Moreover, cathodic activity on the IMP surface generates local alkaline environments [7,43,47], which destabilize the passive oxide layer and promote lateral trench propagation [6,46].

As with AA2024, several forms of local events are also visible on the surface of AA7075. These include (1) dealloying of IMPs with associated trenching, visible as grey centres surrounded by dark rings (see black arrows in Fig. 2a-7200 s); (2) corrosion product deposition, seen as irregular dark grey areas around clusters of corroded particles (see orange arrows in Fig. 2a-7200 s); and (3) streaking corrosion, observed as elongated patches aligned with surface scratches (see magenta arrows in Fig. 2a-7200 s). The streaking corrosion is associated with the dissolution of an altered surface layer rich in Zn and Mg. It is produced by the high shear strains during mechanical grinding and polishing of the AA7075 surface [16,17]. This type of corrosion spreads quickly across the metal surface, as demonstrated by the activity evolution in Movie 1 and as discussed in detail in our recent work [15].

Local activity maps in Fig. 2b show how local corrosion in AA7075 (Area 1 and Area 2) and AA2024 (Area 3 and Area 4) evolved with time. It is noted that these activity maps are still frames from Movie 1. Area 1 activity maps show that some IMPs at the AA7075 surface activated during the first 60 s of immersion. At around 300 s, these particles show signs of extensive trenching based on the development of high activity on their periphery (see cyan arrows in Fig. 2b-Area 1 @ 300 s). Local corrosion progression resulted in visible corrosion product deposition around the particles at around 1800 s. Cathodic reactions on the dealloyed IMPs and dissolution of their adjacent matrices continued with further immersion resulting in wide trenches and substantial corrosion product deposition at 7200 s. Area 2 shows similar local corrosion behaviour as Area 1 except for the appearance of streaking corrosion between 600 and 1800 s (see cyan arrows in Fig. 2b-Area 2 @ 1800 s). Area 3 and Area 4 activity maps also show development of activity associated with IMP dealloying during the first 60 s of immersion. This is consistent with the onset of IMP dealloying reported in previous works for AA2024 [8,43]. Particles from both areas exhibited an increase in activity level and surface spreading with time indicative of dealloying progressing into trenching of the matrix adjacent to the particles. Further dissolution of the matrix led to corrosion product deposition beginning around 1800 s and continuing until the end of immersion.

OCP measurements of the AA2024 and AA7075 surfaces were taken sequentially (i.e., first monitoring AA2024 until 4800 s and then monitoring the AA7075 until the end of immersion) as shown in Fig. 3. The AA2024 OCP is around −0.5 V vs. Ag/AgCl while that of the AA7075 is around −0.65 V vs. Ag/AgCl. The AA2024 OCP is within the range of the previously reported OCP values for AA2024 [8,48] while that of the AA7075 is slightly more positive than the previously reported AA7075 OCP values (i.e., ~ −0.75 V vs Ag/AgCl for 3.5 wt % NaCl [13], ~ −0.8 V vs Ag/AgCl for 0.1 M NaCl [49]). This more positive AA7075 OCP is probably due to the higher contribution of intermetallic particle surfaces like Al_7Cu_2Fe which have been reported to have more positive corrosion potentials (~ −0.5 V vs Ag/AgCl) [50]. The potential difference of the OCPs of the alloys nonetheless highlights that there is a risk of galvanic corrosion when they are electrically connected, with AA2024 likely acting as the global cathode and AA7075 as global anode.

3.2. *Impact of galvanic coupling on local corrosion of AA2024 and AA7075*

Fig. 4a presents the galvanic current density (j_{gal}) and potential (E_{gal}) measured from two trials of 2-h immersion tests in 0.05 M NaCl with the alloys in the assembly externally connected via a ZRA. Analysis of the j_{gal} and E_{gal} will be covered in a subsequent section. The non-zero j_{gal} values indicate electron flow between the two alloys in the assembly. Furthermore, the negative j_{gal} values suggest that the electron flow is from AA7075 (i.e., anode) to AA2024 (i.e., cathode), as expected from the global OCPs of the two alloys (Fig. 3).

The microscopy images corresponding to the galvanically-coupled (GC) alloys at the end of the immersion are shown in Fig. 4b and Fig. 4c. The evolution of the surface activities of the AA2024 and AA7075 from these trials is shown in Movie 2 and Movie 3, respectively.

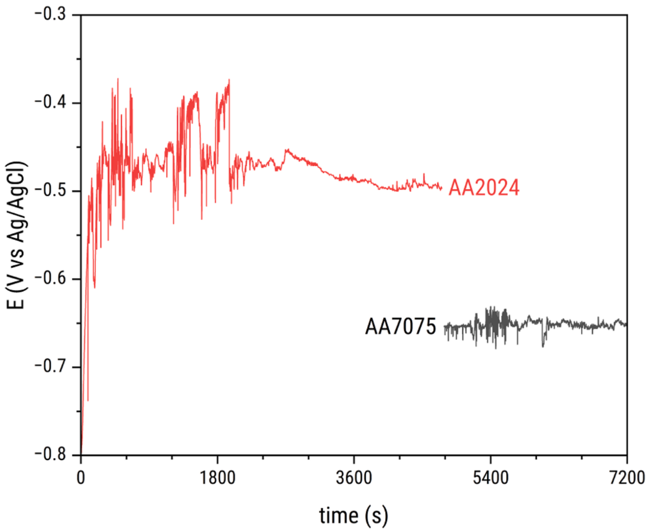

Fig. 3. OCP measurements for AA2024 and AA7075 during the immersion shown in Fig. 2. The OCP measurements of the two surfaces were performed one at a time. The AA2024 surface was measured during the first ~4800 s while that of the AA7075 from ~4800 s to 7200 s.

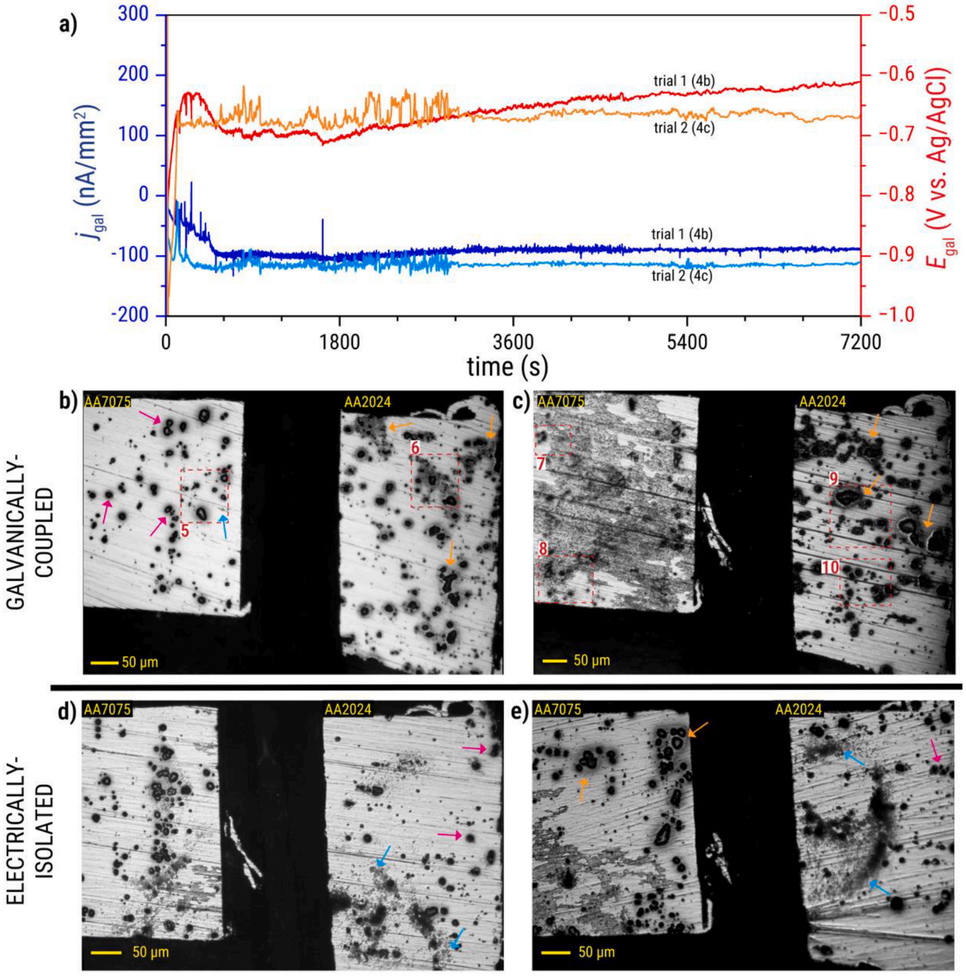

Fig. 4. (a) Galvanic current and potential measured during 2-hour immersion tests in 0.05 M NaCl for two trials of galvanically-coupled AA2024 and AA7075 samples. The alloys were electrically connected via a zero resistance ammeter. Reflected light microscopy images at the end of immersion are shown for (b) trial 1 and (c) trial 2, highlighting the extent of surface corrosion under galvanic conditions. (d) and (e) show microscopy images from two separate trials conducted under electrically-isolated conditions in the same electrolyte.

It is noted that these trials are repeats of the 2-h galvanically-coupled immersion test in 0.05 M NaCl. For reference, reflected microscopy images of the assembly after 2-h immersion tests in 0.05 M NaCl under EI conditions are also presented in Fig. 4d and Fig. 4e. It is noted that the image in Fig. 4d is from the same test as Fig. 2. The end-of-immersion images show that the GC alloys exhibit localized corrosion around intermetallic particles (i.e., dealloying and trenching), similar to that observed for the alloys immersed in EI conditions.

A closer look shows that changes in behaviour attributable to galvanic coupling are most apparent on the AA2024 side of the assembly. These changes include: (1) more widespread dark gray areas surrounding the trenches – referred to here as beyond-trench (BT) activity (see orange arrows in Fig. 4b and Fig. 4c), and (2) a general decrease in corrosion product deposition across the surface. While BT activity is also seen in some AA2024 particles under EI conditions (see magenta arrows in Fig. 4d and Fig. 4e), it occurs less frequently. Notably, although BT activity shares some visual characteristics with corrosion product deposition, the two can be distinguished by their spatial distribution. BT activity is localized around trenches, whereas corrosion product deposition can occur at locations distant from IMPs, including areas with no visible IMP activity (see cyan arrows in Fig. 4d and Fig. 4e).

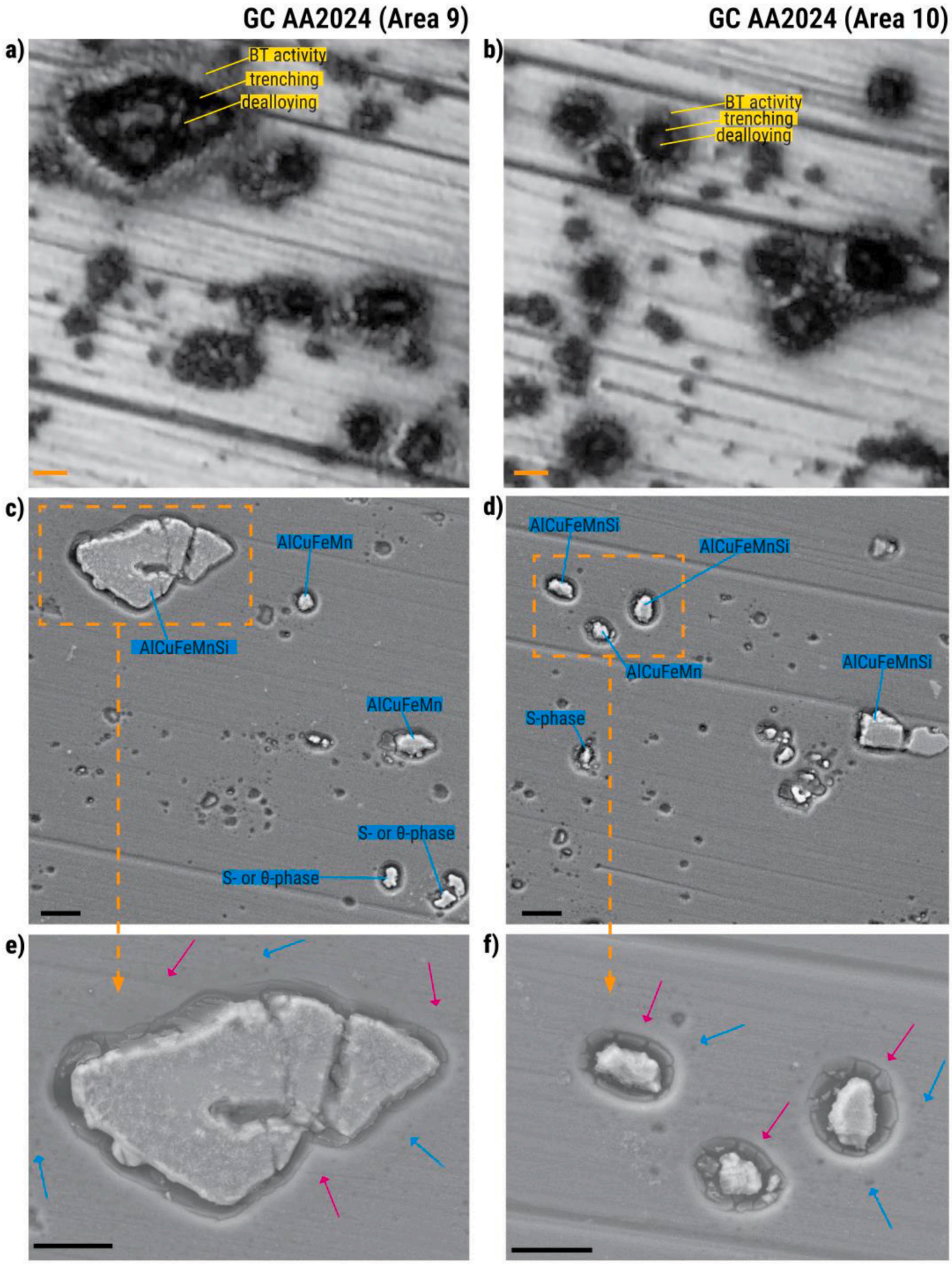

Fig. 5. Close-up light microscopy images of (a) Area 9 and (b) Area 10 from the assembly shown in Fig. 4c after 2 h of immersion. Corresponding post-immersion secondary electron images with IMP composition types identified by EDX are shown in (c) for Area 9 and (d) for Area 10. High-magnification views of selected particles are presented in (e) and (f). Scale bar: 10 μm.

Fig. 5a and Fig. 5b show close-up images of Area 9 and Area 10 on the galvanically-coupled AA2024 surface highlighted in Fig. 4c. Their corresponding post-immersion SEM images are shown in Fig. 5c and Fig. 5d Post-immersion EDX analysis was used to identify the most probable composition type of the IMPs in these areas. The absence of visible deposits around the trenches confirms that BT activity in AA2024 is distinct from corrosion product deposition. Moreover, occurrence of BT activity on both Fe-containing particles (i.e., AlCuFeMnSi, AlCuFeMn) and Cu-rich particles (i.e., S- and θ-phases) suggests that it is not limited by IMP composition. High-magnification images (Fig. 5e and Fig. 5f) of the particles in Fig. 5c and Fig. 5d (see dashed orange rectangles) reveal that BT activity is more consistent with matrix dissolution. The dissolution is observed as smooth areas on the outer side of the trenches (see magenta arrows in Fig. 5e and Fig. 5f). The grooves from grinding and polishing are less distinct on these areas, suggesting that some process evened out the morphological differences. Since no deposits are observed, the smoothing is more likely due to material loss (i.e., dissolution) rather than infill. Apart from the apparent smoothing, dark spots were also observed on the areas corresponding to BT activity (see cyan arrows in Fig. 5e and Fig. 5f). These features are likely related either to local dissolution induced by Cu redeposited from the dealloyed IMPs [6, 7] or attack of dispersoids present around the larger IMP [7].

Extensive dark areas beyond trenches, resembling BT activity observed in this study, have also previously been reported in the AA2024 side of friction-stir welded AA2024-AA7475 under cathodic polarization [40], and in AA2024 corroding in alkaline solutions (pH = 10) [51]. Similar to bulk alkaline solutions, cathodic polarization of IMPs generates local alkalinity near the IMP surface through the oxygen reduction reaction. Both scenarios suggest that BT activity is pH-driven and may represent an extension of the same processes responsible for lateral trench propagation. The broader extent of dissolution beyond trenches under GC conditions suggests that galvanic coupling of the two alloys may have enhanced the local alkaline environment around the AA2024 IMPs compared to EI conditions. Such enhancement potentially explains the observed extent of local corrosion reported on the AA2024 side of friction-stir welded AA2024-AA7475 after a 24-h immersion in 0.01 M NaCl under open-circuit conditions [40], and on the AA2024 side of friction-stir welded AA2024-AA7075 after a 12-h immersion in 3.5 wt % NaCl also under open-circuit conditions [52]. Furthermore, the development of the local alkaline environment also explains the delayed acidification of the AA2024 side observed during pH variation tests for friction-stir welded AA2024-AA7475 [41].

The corrosion of the AA7075 side under GC conditions is more varied than that of AA2024, particularly in terms of the extent of streaking corrosion. The AA7075 sample from trial 1 exhibited dealloying events accompanied by extensive trenching and limited streaking corrosion (see cyan arrow in Fig. 4b). Dark gray areas (i.e., BT activity) around the trenches are also observed (see magenta arrows in Fig. 4b), although not as extensive as that in the AA2024 surface. Similar behaviour is observed in some of the AA7075 IMP clusters immersed under EI conditions (see orange arrows in Fig. 4e). Although SEM images of these sites are not available, post-immersion SEM analysis of IMPs from another AA7075 sample immersed in similar conditions (Fig. 6) shows that this kind of darkening is due to dissolution, not corrosion product build-up. On the other hand, the AA7075 sample from trial 2 (Fig. 4c) exhibited extensive streaking corrosion which impacted almost the entire surface, in addition to the dealloying and trenching around IMPs. A closer look at the microscopy and post-immersion SEM images of Area 7 and Area 8 on the AA7075 surface (Fig. 7) shows features of streaking corrosion, as well as dealloying and trenching around IMPs. Although the surface changes due to streaking corrosion registered substantial activity levels, the SEM images of the streaked areas show that the streaking corrosion depth is barely perceptible. In Fig. 7a, the streaked area on the right side of the SEM image has a patchy texture with slight darker colour than the unstreaked matrix. The same patchy texture is observed in the SEM images of the streaked areas in Fig. 7b. Apart from the streaking, the trenching appears to be less extensive than that observed for the AA2024 IMPs under GC immersion (Fig. 5) or the AA7075 IMPs under EI immersion (Fig. 6). Post-immersion EDX analysis of the IMPs marked in Fig. 7b indicates that particles 1, 2, and 3 are Fe-rich while particles 4 and 5 are Cu-rich. Interestingly, the Cu-rich particles registered higher Zn atomic percentages than the Fe-rich particles or the AA7075 matrix. This suggests considerable Zn precipitation on the more active particles of AA7075, which may influence the extent of cathodic reactions on the IMP surface.

Overall, the corrosion on the AA7075 surfaces in both GC trials appears comparable to that observed in the EI trials (Fig. 4d and Fig. 4e). The AA7075 IMPs in the EI trials also exhibited dealloying and trenching combined with varying degrees of streaking corrosion. IMPs from both GC and EI conditions also exhibited some degree of BT activity. The similarities suggest that while galvanic coupling had visible effects on AA2024, its impact is less distinct on the AA7075 side despite the negative galvanic currents measured.

3.3. Local corrosion progression of galvanically-coupled AA2024 and AA7075

The progression of local corrosion on AA7075 and AA2024 IMPs was examined in detail to understand how the final states shown in Fig. 4b and Fig. 4c developed. Due to variation in the extent of streaking between the two GC immersion trials, their local corrosion behaviour was analysed separately.

Local activity maps in Fig. 8 show time-resolved local surface changes in Areas 5 and 6 (Fig. 4b) of the first trial of the GC immersion. The maps are still frames of Movie 2. As with the uncoupled system in Fig. 3, activity initiation associated with dealloying was observed on area 5 in the early stages of immersion (Fig. 8a – 60 s). This gave way to dissolution of the adjacent matrix seen in some particles as higher

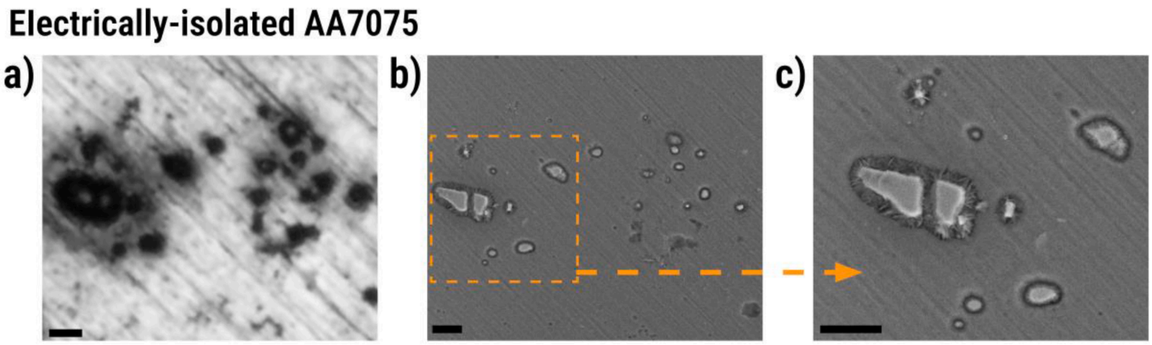

Fig. 6. (a) Reflected light microscopy image of IMPs immersed in electrically-isolated conditions, and their corresponding post-immersion (b, c) secondary electron images showing that the dark gray areas surrounding the trenches have no visible corrosion product deposition. These images are from another AA7075 sample immersed in 0.05 M NaCl for 2 h. Scale bar indicates 10 μm.

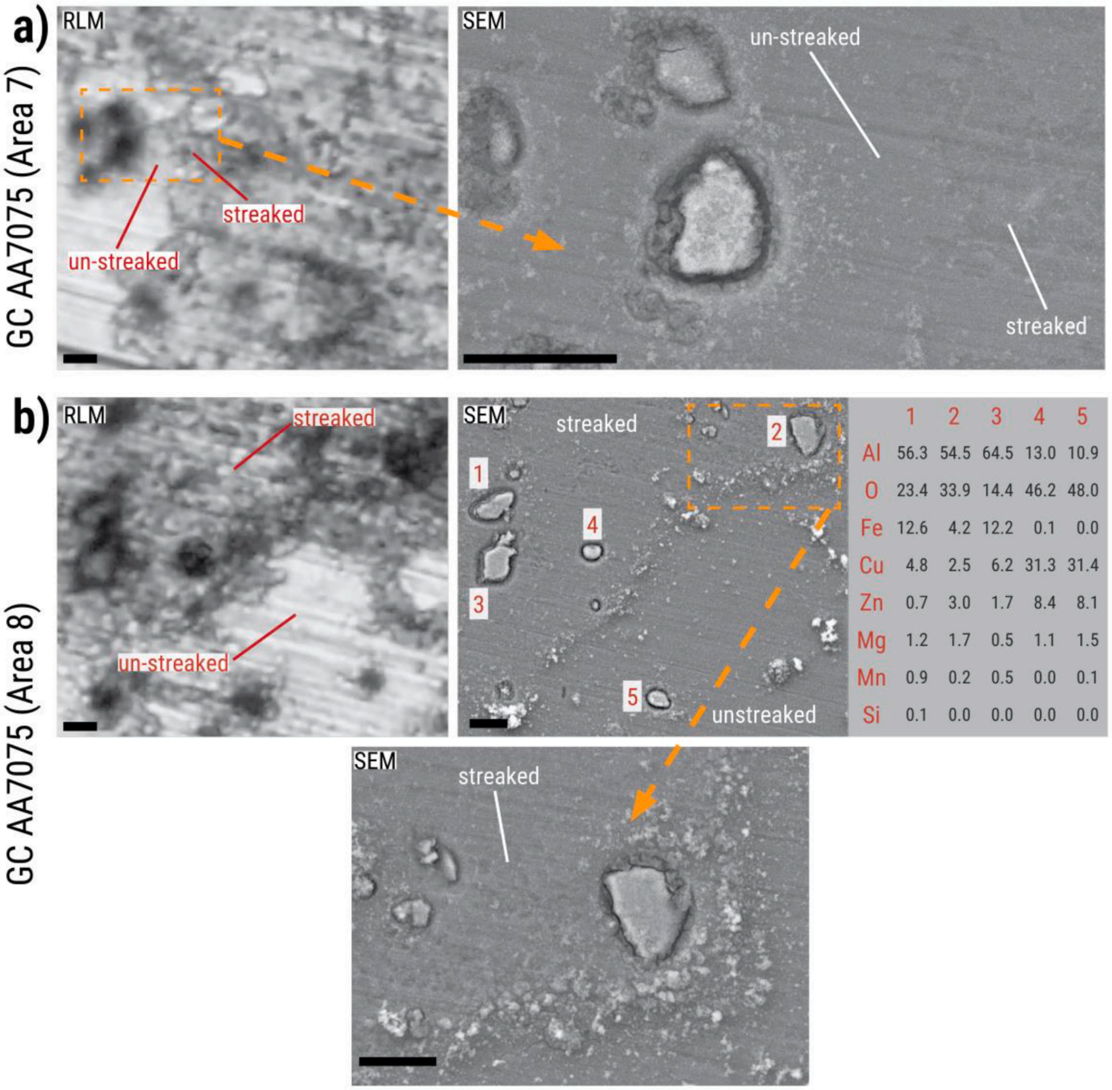

	1	2	3	4	5
Al	56.3	54.5	64.5	13.0	10.9
O	23.4	33.9	14.4	46.2	48.0
Fe	12.6	4.2	12.2	0.1	0.0
Cu	4.8	2.5	6.2	31.3	31.4
Zn	0.7	3.0	1.7	8.4	8.1
Mg	1.2	1.7	0.5	1.1	1.5
Mn	0.9	0.2	0.5	0.0	0.1
Si	0.1	0.0	0.0	0.0	0.0

Fig. 7. Close-up reflected light microscopy images of (a) Area 7 and (b) Area 8 from the galvanically coupled assembly in Fig. 4c after 2 h of immersion, with corresponding post-immersion SEM images. These show streaking corrosion features and the extent of dealloying and trenching around IMPs. Post-immersion EDX compositions of the particles are also shown for (b). Scale bars: 10 μm.

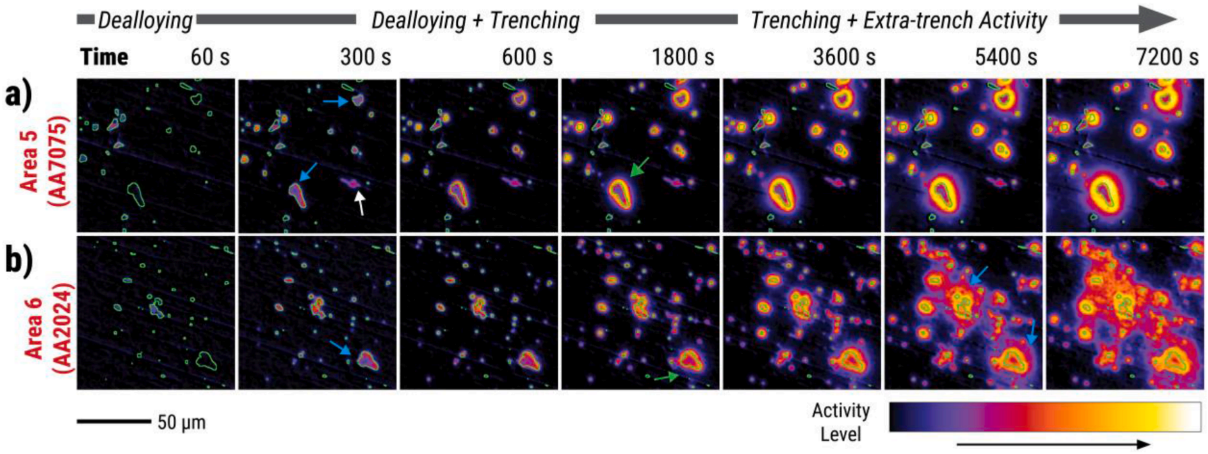

Fig. 8. Time-resolved activity maps showing localized corrosion sites on (a) Area 5 and (b) Area 6 from the AA7075 and AA2024 surfaces in the assembly shown in Fig. 4b Green overlays indicate intermetallic particle boundaries used for analysing intermetallic activity. Warmer colours indicate higher activity levels.

activity on the IMP edge (see cyan arrows in Fig. 8a – 300 s) or as an increase of the active area in others. A short-lived streaking corrosion event was also recorded between 60 and 300 s (see white arrow at 300 s in Fig. 8a). The trenches around the IMPs continued growing with further immersion and was observed as increase in both activity level and width of the trenched areas. At around 1800 s, BT activity (i.e., purple zones around the warm-coloured trenches) developed around some IMPs (see green arrows in Fig. 8a). As with the trenches, these BT areas exhibited an increase in both activity level and affected area with further immersion. Notably, the growth of the trenches appears to slow down as there is a less pronounced change in the width of the trenches (yellow-coloured areas in the Fig. 8a maps) between 1800 s and 7200 s. Comparable sequence of local corrosion events was observed in Area 6: IMP dealloying in the first minutes (Fig. 8b – 60 s) followed by trenching (see cyan arrows in Fig. 8b – 300 s) and then BT activity onset (see green arrows at 1800 s in Fig. 8b). At around 5400 s, BT activity (see cyan arrows in Fig. 8b – 5400 s) reached considerably high levels (i.e., reddish-orange in the activity level colour scale) indicating intensification of the underlying process.

Similar corrosion features were observed in the second GC immersion trial, even though the AA7075 surface showed more extensive streaking corrosion than in the first trial. Fig. 9a and Fig. 9b show activity maps for Areas 7 and 8 (AA7075) from the second trial, taken as still frames from Movie 3. The activity maps of both areas exhibit the spread of streaking corrosion, first appearing in Area 7 at 600 s and in Area 8 at 300 s (see white arrows). It eventually dominated surface activity and affected the visibility of other local corrosion events on the surface before ending between 1800 s and 3600 s (see Movie 3). Apparent BT activity was observed in one particle from around 1800 s (see cyan arrow in Fig. 9b–1800 s). However, identifying BT activity in other AA7075 IMPs was more difficult due to the extent of streaking corrosion on the surface. On the AA2024 side, Areas 8 and 9 (Fig. 9c, d) showed a corrosion sequence comparable to the first trial: early-stage IMP dealloying and trenching followed by BT activity development (see cyan arrows in Fig. 9c, d–3600 s). The BT activity became substantially high with further immersion leading to a similar appearance to some of the trenches (see cyan arrow in Fig. 9b, c–7200 s). It is noted that the activity maps for areas 8 and 9 correspond to the end-of-immersion microscopy images and post-immersion SEM images shown in Fig. 5.

A visible drop in activity was observed on the streaked regions of Areas 7 and 8 between 3600 s and 5000 s (Fig. 9a, b). This suggests changes on the already-streaked areas. The reduction in activity is potentially due to the release of nanograin remnants of the altered surface layer to the solution [14]. This loss of grain remnants likely reduced the roughness of the surface resulting in a decrease in the degree of light scattering and a corresponding drop in the pixel activity levels. Interestingly, this reduction in activity is most apparent in the streaked areas farther from the IMP sites. A further drop in apparent activity between 5000 and 7200 s is due to changes in lighting conditions.

The overall local corrosion progression in both trials can be summarized in three stages based on the optically-dominant process: (Stage 1) dealloying-dominated stage, (Stage 2) trenching-dominated stage (with varying degrees of streaking corrosion), and (Stage 3) BT activity-dominated stage. Interestingly, both Stage 1 and Stage 2 were also observed in the uncoupled systems (Fig. 2). Some form of Stage 3 was also seen in certain IMPs from the EI tests but they more closely resembled the BT activity observed in the AA7075 side of the GC assembly (i.e., uniform and low-level activity) than the high activity seen in AA2024 under GC conditions. These similarities between the GC and EI systems indicate that the local corrosion stages identified are not exclusive to GC systems. Despite the similarities, Stage 3 in the AA2024 side of the GC system developed more aggressively than that of the AA2024 in the EI system. This suggests that galvanic coupling of AA2024 and AA7075 does not change which stages occur, but likely increases the rate and severity of their progression, as will be analysed in the following section.

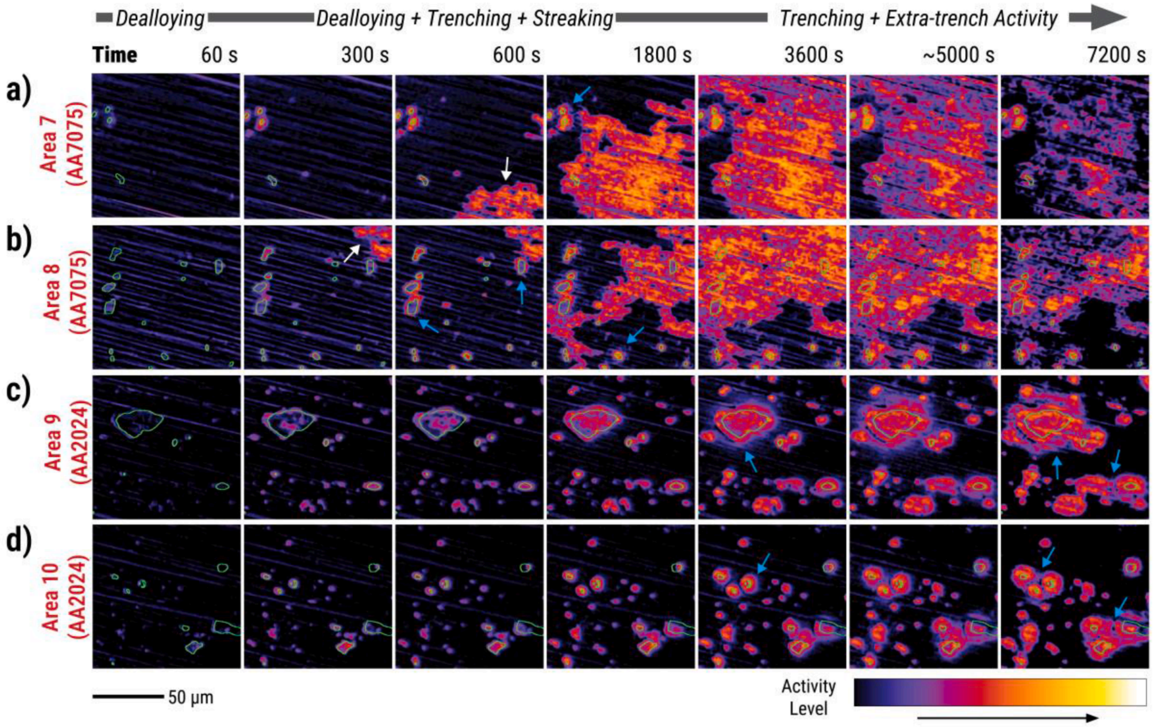

Fig. 9. Time-resolved activity maps showing localized corrosion sites on (a) Area 7, (b) Area 8, (c) Area 9, and (d) Area 10 from the AA7075 and AA2024 surfaces in the assembly shown in Fig. 4c. Green overlays indicate the boundaries used for analysis of IMP activity. Warmer colours indicate higher activity levels. The drop in the apparent activity of the matrix between 5000 and 7200 s is due to changes in the lighting conditions.

3.4. Kinetics of local corrosion processes in AA2024-AA7075 couple

Kinetic descriptors for the stages of local corrosion (i.e., dealloying-dominated, trenching-dominated, BT activity-dominated) were extracted from the local activity maps to assess the potential impact of galvanic coupling between AA2024 and AA7075. The descriptors are extracted from the simplified pixel activity level distribution (sPAD) plots (see the sample plot in Fig. 10a) for the pixels within the IMP boundary. The descriptors include the onset of rapid activity increase on the IMP (t_{onset}) and the dealloying-to-trenching transition point (t_{tp}). Fig. 10a shows a sample plot marking how these values were extracted. The t_{onset} is associated with the start of dealloying and can be used to estimate the beginning of Stage 1. The t_{tp} indicates where the rapid activity increase begins slowing down and marks the shift from Stage 1 to Stage 2 [8]. As shown in the local activity maps corresponding to the sample sPAD (Fig. 10b), there is still some degree of dealloying during Stage 2. However, the trenching process contributes most to the activity level increase as well as the spread of active areas. The t_{onset} and t_{tp} values were numerically estimated from the sPADs and are subject to the tolerances used for estimation. In cases wherein there is noise or discontinuities in the data, the values of the parameters were manually estimated through a combined analysis of the sPADs and visual inspection of the activity maps. Additional details of the estimation procedure are provided in Supporting Information 3.

The t_{onset} distributions (Fig. 11a) for AA2024 were nearly identical: 33 ± 23 s under GC conditions and 21 ± 19 s under EI conditions. Similarly, AA7075 showed comparable distributions, with a t_{onset} of 45 ± 44 s (GC) and 52 ± 54 s (EI). The high standard deviations are expected, since the t_{onset} values reported come from particles of varying composition. The t_{tp} distributions (Fig. 11b) were also comparable between the EI and GC conditions. For AA2024, the mean t_{tp} values were 181 ± 61 s (GC) and 171 ± 49 s (EI), while AA7075 showed values of 223 ± 73 s (GC) and 214 ± 73 s (EI). Comparable t_{onset} and t_{tp} distributions for EI and GC conditions suggest that galvanic coupling had minimal effect on the dealloying-dominated stage (Stage 1). Activity level increase rates can also be calculated for the period between t_{onset} and t_{tp}. These values are presented in Supporting Information 3 and also indicate comparable Stage 1 behaviour for IMPs in EI and GC immersion conditions.

The effect of galvanic coupling on the subsequent trenching-dominated stage (Stage 2) was examined by selecting regions of interest that match the full width of the trenches seen at the end of immersion (Fig. 12a). To isolate trench behaviour, a mask was applied to exclude the IMP pixels, so only the area covered by the trench was analysed. As the trench grows, more pixels reach higher activity levels. A threshold of 5 was used to identify active pixels while minimizing noise. The number of active pixels indicates the expanding trench area. Once the trench fully spans the region of interest, the number of active pixels levels off. The point when this plateau occurs is defined as the trench full-width time (t_{fwt}). This t_{fwt} not only marks the completion of the trench's lateral growth but also helps to indicate when BT activity might begin. After t_{fwt}, further increase in activity within the trench area mainly reflects deepening while activity spreading beyond the trench is attributed to the onset of BT activity (Fig. 12b). It is noted that the current method for estimating t_{fwt} is less accurate for small trenches because the resolution of the imaging system starts to affect the distinction between IMP pixels and trench pixels.

Fig. 13a and Fig. 13b compare the t_{fwt} distribution as a function of trench area (i.e., the estimated area of the trench surrounding particle) for IMPs in AA2024 and AA7075, under both EI and GC conditions. For AA7075 (Fig. 13a), galvanic coupling (orange dots) resulted in relatively lower t_{fwt} values (GC t_{fwt} mean: 1132 ± 559 s, EI t_{fwt} mean: 2232 ± 1154 s) than EI conditions (blue squares) particularly for bigger trenches (i.e., above ~40 μm^2). This suggests that, on average, AA7075 trenches under GC conditions reached their full width earlier (i.e., in around half the time) than those in EI conditions.

As for AA2024 (Fig. 13b), the overall distribution of t_{fwt} from the GC trials is slightly earlier than that from the EI conditions (GC t_{fwt} mean: 2202 ± 1182 s, EI t_{fwt} mean: 2926 ± 1752 s). Moreover, when the GC data are separated with the extent of streaking in mind, the t_{fwt} values from trial 1, which had limited streaking, appear lower (2407 ± 1153 s) than those from trial 2 (3055 ± 1293 s), which had extensive streaking. The trial 1 t_{fwt} values suggest that galvanic coupling potentially accelerated trench propagation in AA2024 IMPs. However, the trial 2 t_{fwt} values suggest that the trench propagation of AA2024 IMPs was slower when there was extensive streaking corrosion on the AA7075 side. Identification of a slow down of trenching on the AA7075 side is difficult to confirm due to the extensive streaking corrosion.

The t_{fwt} values indicate that the onset of BT activity (Stage 3) for most IMPs in the GC system happened within the first hour of immersion. This suggests that for most of the immersion period, the local corrosion processes happening on the surface of the alloys were a mixture of trench deepening and BT activity propagation. Both of these processes are forms of matrix dissolution. Quantitative analysis of BT propagation poses some challenges because it often involves overlapping areas from multiple IMPs, especially when they are clustered. Additionally, BT activity can sometimes be indistinguishable from corrosion product deposition and requires additional context (e.g., SEM data) to resolve the differences.

3.5. Galvanic current density and potential of AA2024-AA7075 couple

The j_{gal} and E_{gal} trends measured during immersion reflect the overall electrochemical response to localized corrosion processes described in Sections 3.2 and 3.3. Changes in these signals over time are directly linked to the initiation and progression of dealloying, trench

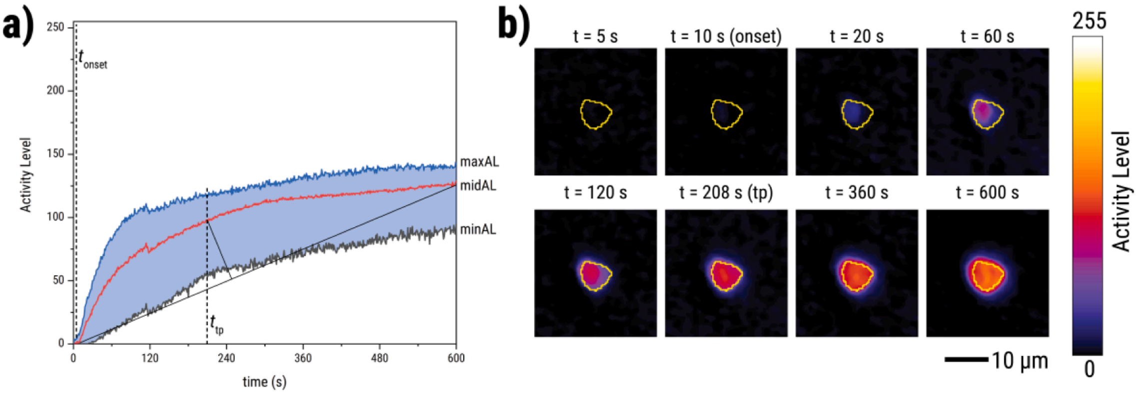

Fig. 10. (a) Simplified pixel activity level distribution plot during the initiation of activity in an intermetallic particle, and (b) the corresponding local activity maps showing the corresponding surface changes at different points in time around the characteristic times (i.e., t_{onset}, t_{tp}) extracted from the plot.

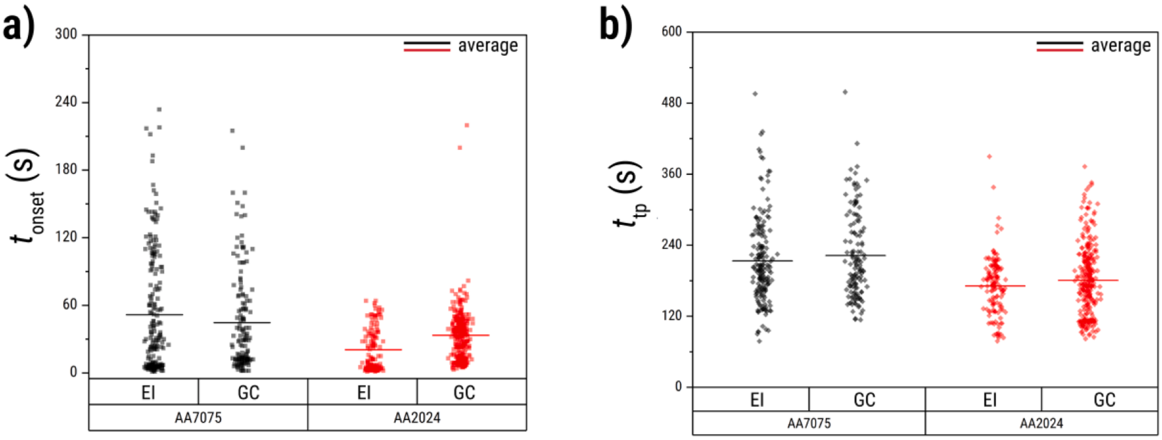

Fig. 11. (a) Onset time of dealloying and (b) time of transition from dealloying-dominated to combined trenching and dealloying, for AA7075 and AA2024 particles. Results are shown for both electrically-isolated (EI) and galvanically-coupled (GC) conditions in the assembly (1:1 area ratio).

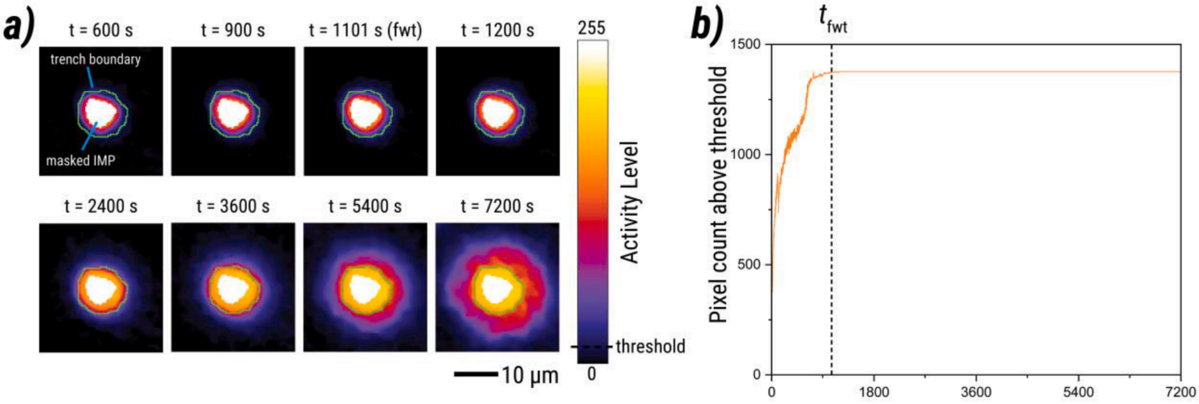

Fig. 12. (a) Local activity maps showing surface changes at different times around the trench full-width time (t_{fwt}). A white mask is applied to the IMP pixels in order to focus the analysis on the spreading trench. The green boundary corresponds to the coverage of the trench defined from end-of-immersion optical observations. (b) Number of pixels inside the trench boundary with activity level above the threshold of 5 plotted against time used for estimating t_{fwt}.

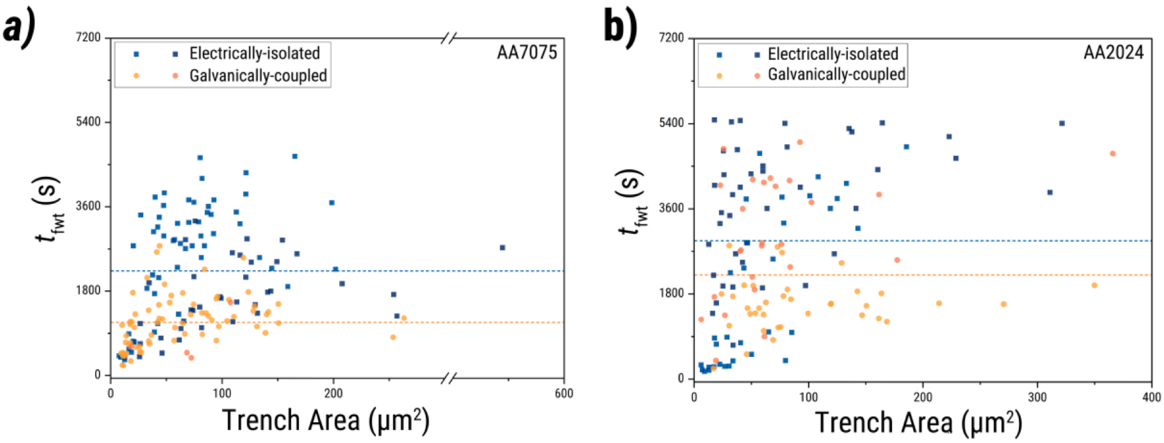

Fig. 13. Estimated trench full-width time (t_{fwt}) for intermetallic particles in (a) AA7075 and (b) AA2024 under electrically-isolated and galvanically-coupled conditions. The area ratio between AA2024 and AA7075 is 1:1. Different shades (e.g., light blue and dark blue) represent values from different experimental trials. The dashed lines indicate the average t_{fwt} of electrically-isolated and galvanically-coupled data points.

formation, and BT activity on the AA2024 and AA7075 surfaces. To better understand how these local corrosion events developed under GC conditions, the E_{gal} and j_{gal} behaviour are examined in relation to the three main stages of localized corrosion: Stage 1 (dealloying-dominated), Stage 2 (trenching-dominated), and Stage 3 (BT activity-dominated). The distribution of optics-based characteristic times (Fig. 14a, Fig. 15a) were aligned in time with the E_{gal} and j_{gal} curves (Fig. 14b, Fig. 15b) to correlate the microscopy data with the electrochemical data.

In trial 1 (Fig. 14), E_{gal} ranged between approximately −0.7 and

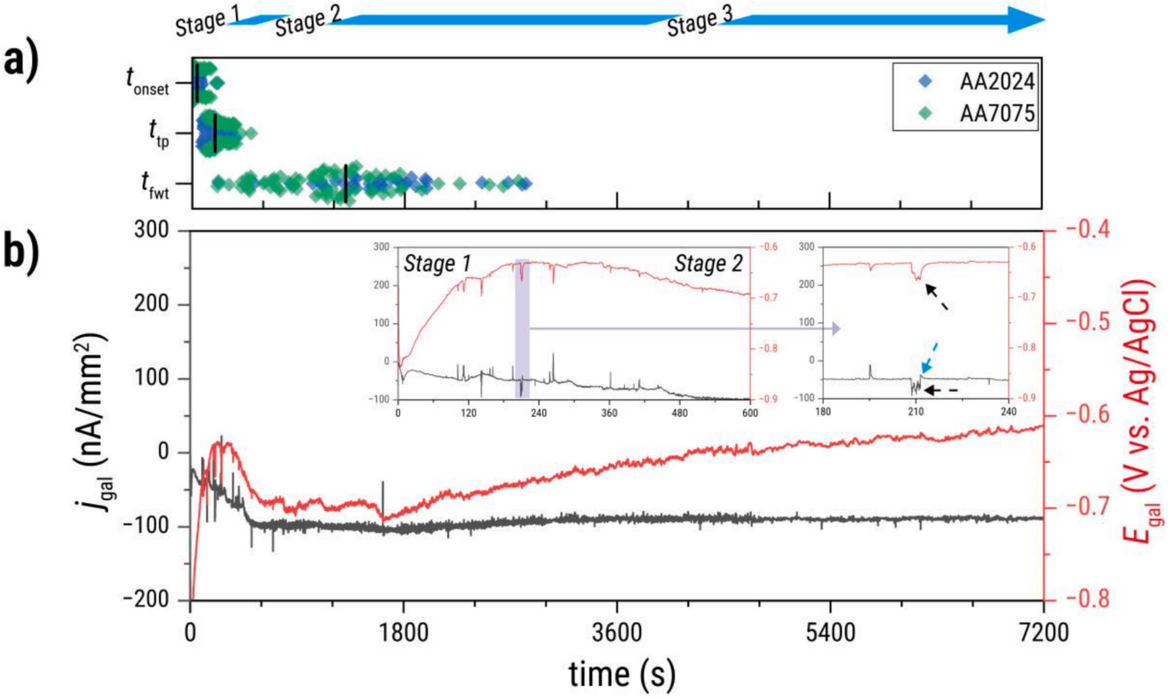

Fig. 14. Time-aligned (a) optics-based kinetics parameters (t_{onset}, t_{tp}, t_{fwt}) and (b) galvanic potential and current density for trial 1 of the galvanically-coupled immersion shown in Fig. 4b and Fig. 8.The black vertical bars in (a) indicate the mean of the kinetic parameter. The insets in (b) show the first 600 s of immersion and a magnified section corresponding to the streaking corrosion.

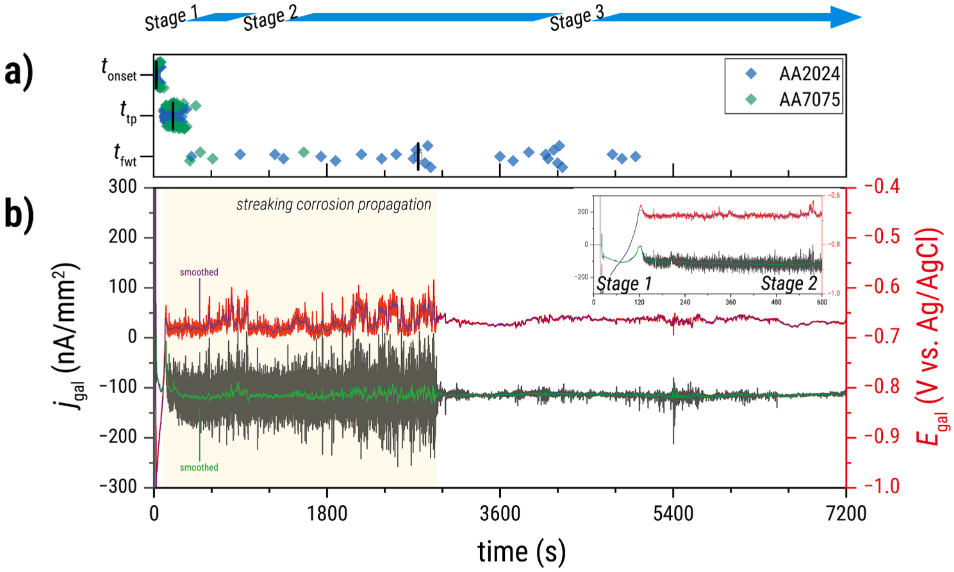

Fig. 15. Time-aligned (a) optics-based kinetics parameters (t_{onset}, t_{tp}, t_{fwt}) and (b) galvanic potential and current density for trial 2 of the galvanically-coupled immersion shown in Fig. 4c and Fig. 9.The black vertical bars in (a) indicate the mean of the kinetic parameter. High-frequency high-amplitude transients between 0 and 3000 s are due to streaking corrosion propagation on the surface of the AA7075 alloy.

−0.6 V vs. Ag/AgCl. This is more negative than the OCP of AA2024 and slightly more positive than that of AA7075, consistent with a mixed potential arising from galvanic coupling between the two alloys. As previously shown in Fig. 4a, the negative j_{gal} values indicate electron flow from AA7075 to AA2024. Electrochemical signal trends of the trial 1 assembly in each local corrosion stage are as follows:

- **Stage 1 (trial 1):** The dealloying-dominated stage occurred between 0 and approximately 193 s, based on the average t_{tp} values of the sampled IMPs from both AA2024 and AA7075 (Fig. 14a). This stage is mainly driven by dealloying, as supported by the t_{onset} distribution, which mostly falls within this time range (with an average t_{onset} of 41 s). During this period, E_{gal} gradually shifted to more positive values with only minor fluctuations (transients), while j_{gal} steadily became more negative, indicating increasing electron flow between the two alloys.
- **Stage 2 (trial 1):** The trenching-dominated stage is estimated to begin around 193 s and transition to the next stage around 1300 s - the average t_{fwt} of sampled trenches from both AA2024 and AA7075 (Fig. 14a). During this stage, E_{gal} exhibited a change in trend and

began a drift to more negative values, which reflected increased anodic activity specifically associated with the growth of trenches around the IMPs. The drift was accompanied by several high-amplitude transients, predominantly in the negative direction, with amplitudes up to ∼40 mV. Meanwhile, j_{gal} exhibited a shift to more negative values and exhibited transients with amplitudes up to ∼100 nA mm^{-2}. It is noted that the E_{gal} transients matched the timing of the j_{gal} transients. The j_{gal} drift to more negative values suggests that the increase in anodic activity is more extensive for the AA7075 surface, leading to increased electron flow from AA7075 to AA2024.

One of the transients in this stage (see dashed black arrows in the magnified inset in Fig. 14b) corresponds to the brief streaking corrosion (see white arrow in Fig. 8a – 300 s) observed from 208 s to 213 s. The E_{gal} transient sequence during this event is consistent with the streaking corrosion behaviour reported in our previous work [15], characterized by an almost instantaneous potential drop, followed by high-frequency transients, and then a gradual return to the pre-streaking potential. The initial potential drop and the subsequent high-frequency transients are attributed to the anodic nature of the streaking initiation and propagation (i.e., dissolution of Zn and Mg [14,15]) dominating the electrochemical response of the surface. The return to the pre-streaking potential is interpreted as the system's relaxation to a state wherein the cathodic reactions are balanced by the other dissolution processes on the IMPs and on the trenches [15]. A comparable response was observed in j_{gal}: an initial current drop, followed by high-frequency fluctuations, and then a return to pre-streaking levels. The initial drop indicates increase electron flow from AA7075 to AA2024 and is consistent with the presence of a dominating anodic process on AA7075. The high-frequency fluctuations reflect the electron flow from the streaking propagation. The return to pre-streaking levels corresponds to the termination of the anodic process associated with streaking corrosion. Interestingly, the j_{gal} trend corresponding to streaking corrosion termination is not smooth like that of E_{gal}. Instead, j_{gal} overshoots slightly and goes above the pre-streaking level before coming back down (see dashed cyan arrow in Fig. 14b inset). This overshoot suggests that streaking corrosion termination causes a temporary decrease in the current from AA7075 to AA2024. The exact cause of this overshoot is not yet known and is recommended for further investigation.

- **Stage 3 (trial 1):** The BT activity-dominated stage is estimated to begin around 1300.3 s (Fig. 14a). As more particles transition into Stage 3, a corresponding E_{gal} shift to more positive values (i.e., closer to AA2024 OCP) is observed. This trend suggests an overall ennoblement of the assembly. The shift was accompanied by low amplitude transients (up to ∼10 mV). Meanwhile, j_{gal} exhibited a slight drift to less negative values combined with low amplitude transients (up to 20 nA mm^{-2}) around the same time.

E_{gal} and j_{gal} measurements from the second trial (Fig. 15) showed comparable behaviour to that of the first trial. The E_{gal} also ranged between approximately −0.7 and −0.6 V vs. Ag/AgCl and its j_{gal} was persistently negative as previously shown in Fig. 4a. The E_{gal} and j_{gal} trends for trial 2 at each local corrosion stage are as follows:

- **Stage 1 (trial 2):** The dealloying-dominated stage occurred between 0 and approximately 199 s (i.e., average t_{tp} from both AA2024 and AA7075). All of the dealloying onsets of the sampled IMPs from both alloys fall within this period (average $t_{onset} = 29$ s). As with trial 1, E_{gal} gradually shifted to more positive values with minimal transients. The j_{gal} was also generally noise-free and initially drifted to more negative values before slightly shifting to more positive values.
- **Stage 2 (trial 2):** The trenching-dominated stage is estimated to begin around 199 s and transition to the next stage around 3056 s (the average t_{fwt} of sampled trenches from both AA2024 and AA7075). However, well-defined E_{gal} and j_{gal} trends are not observed during this stage for trial 2 due to massive streaking corrosion initiation and propagation. The streaking corrosion also limited analysis of trenching events in trial 2 resulting in a low number of AA7075 t_{tp} data points. Similar to the streaking corrosion event documented in trial 1, the streaking corrosion event in trial 2 leads to a drop in E_{gal} and j_{gal} to more negative values. The more negative E_{gal} is consistent with the anodic nature of streaking corrosion. Meanwhile, the more negative j_{gal} indicates that the streaking corrosion in this trial also increased the electron flow to AA2024. Due to the prolonged streaking during this test, the high-frequency fluctuations also became much more apparent. The smoothed j_{gal} curve (green curve in Fig. 15b) shows that the average current density during this period is relatively stable at around −120 nA mm^{2}. The fluctuations, on the other hand, caused j_{gal} to swing between ∼−200 to ∼0 nA mm^{2}. This is consistent with the current density fluctuation briefly observed in trial 1 due to the limited streaking corrosion propagation. Interestingly, the j_{gal} fluctuations exhibit much higher amplitudes as more IMPs transition out of Stage 2. More transient peaks are observed going close to 0 nA mm^{-2} and beyond −200 nA mm^{-2}. Despite the j_{gal} fluctuations, overall negative values indicate that the AA2024 remained the cathode of the couple.
- **Stage 3 (trial 2):** The BT activity-dominated stage is estimated to begin around 3056 s based on the mean t_{fwt} values. Interestingly, this coincides with the termination of streaking corrosion marked by the disappearance of the high-frequency fluctuations in both E_{gal} and j_{gal}. The correlation between the transition from Stage 2 to Stage 3 and the electrochemically measured parameters gives more weight to the GC-accelerated trenching pathway proposed for Stage 2. As more particles transition into stage 3, the E_{gal} also starts gradually shifting to more positive values while exhibiting low amplitude transients (up to ∼10 mV). The E_{gal} shift is not as extensive as that in trial 1. Comparison of the baseline in Stage 2 with that in Stage 3 (see smoothed blue curve in Fig. 15b) shows an increase of around 10 mV between stages. Unlike trial 1, the j_{gal} baseline remained semi-stable during the transition from Stage 2 to Stage 3.

Overall, the electrochemical responses observed across both trials reflect a correlation between the evolving galvanic signals and the progression of localized corrosion processes on the AA2024-A7075 assembly. Both trials yielded comparable Stage 1 electrochemical behaviour. However, the electrochemical patterns became more complex once dissolution of the matrix occurred. The higher magnitude of Stage 2 current densities measured in both tests does show that the galvanic coupling became more established once matrix dissolution is involved. These findings suggest that the evolution of macroscale galvanic interactions between AA2024 and AA7075 is intimately tied to the progression of local corrosion processes. The development of the galvanic measures suggests that IMPs must first activate and then initiate matrix dissolution before substantial macro-galvanic interactions develop.

3.6. *Proposed mechanism of local corrosion in AA2024-AA7075 couple*

A local corrosion mechanism (Fig. 16) is proposed, based on the previously discussed optical and electrochemical observations, to describe how the microstructures of AA2024 and AA7075 interact under galvanic coupling and contribute to the macroscale galvanic interactions observed.

In Stage 1, localized corrosion begins with the dealloying of IMPs in both alloys. During this dealloying-dominated stage, E_{gal} gradually shifts to more positive values, which is consistent with the previously reported behaviour for dealloying in AA2024 under open-circuit conditions [8,53]. This positive shift reflects the ennoblement of the dealloying particles, as they lose their less noble components (e.g., Mg, Zn). The corresponding negative j_{gal} indicates the flow of electrons from AA7075 to AA2024 during this stage. However, its magnitude is still not as large as that observed in the later stages despite the rapid changes observed on

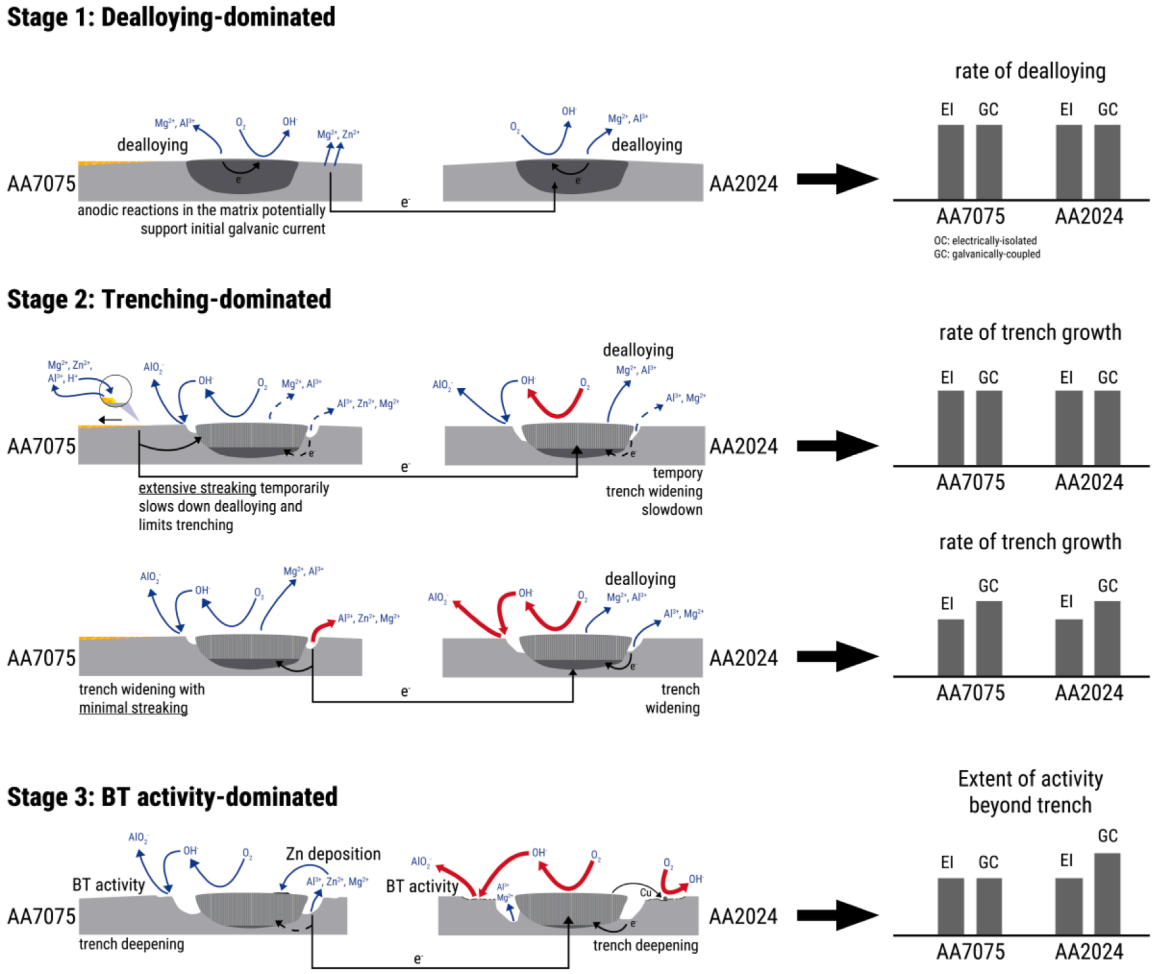

Fig. 16. Proposed mechanism for the progression of localized corrosion under galvanically-coupled (GC) conditions for AA2024 and AA7075, along with a schematic representation of the associated effects on optically-detected surface phenomena. Thick red arrows denote processes that are potentially accelerated relative electrically-isolated (EI) conditions, while dashed arrows indicate processes that may be suppressed or decelerated.

the surface. This suggests that during Stage 1, electron flow from the dealloying and early-stage trenching is still contained to the local corrosion sites and likely has minimal contribution to the macroscale galvanic coupling. Comparable Stage 1 kinetic descriptors (t_{onset}, t_{tp}) for the EI and GC immersion conditions further support this observation. If the galvanic coupling of AA2024 and AA7075 is closely tied to the initial IMP activation, it is reasonable to expect changes in how the particles activate. However, since this is not the case, this raises the question on the nature of the process or processes that contribute to the early-stage galvanic current from AA7075 to AA2024. One potential candidate is the dissolution of anodic particles in AA7075, such as Mg_2Si and $MgZn_2$ [49]. These particles are typically too small to be detected by reflected light microscopy, which limits their visibility in the in situ optical analysis. Another potential pathway is the direct galvanic coupling between the bulk AA2024 and AA7075 matrices resulting in the loss of Mg and Zn from the AA7075 matrix. However, the activity of the matrices is also closely tied to the activation of the IMPs, making it difficult to isolate the changes due to microgalvanic coupling from those due to the galvanic coupling of AA2024 and AA7075.

In Stage 2, local corrosion becomes trenching-dominated, with both AA2024 and AA7075 developing trenches around IMPs due to their microgalvanic coupling with their surrounding matrix. The electrochemical and optical responses during this stage are also influenced by the presence or absence of streaking corrosion on the AA7075 surface. Trenching generally corresponds to the anodic dissolution of the matrix adjacent to the IMPs. As such, in the absence of streaking, the onset of trenching in both AA2024 and AA7075 results in a visible drift of E_{gal} to more negative values (Fig. 14b). The E_{gal} drift is also accompanied by further increase in the magnitude of j_{gal}, which indicates increased electron flow from AA7075 to AA2024. For AA7075, faster widening of trenches was observed in GC systems based on their lower t_{fwt} values (Fig. 13a). The faster widening indicates higher matrix dissolution rates, which could also have contributed to the electron flow between AA7075 and AA2024. Increasing j_{gal} suggests more cathodic activity than anodic activity on the AA2024 side. While the electron flow could potentially passivate the AA2024 matrix, this appears to lead instead to faster trench widening as seen in the lower t_{fwt} of the AA2024 IMPs. This suggests that one aspect of galvanic coupling between AA7075 and AA2024 is potentially between the AA7075 matrix and the AA2024 IMPs. The galvanic current density potentially intensifies the cathodic activity of AA2024, thereby enhancing reactions already occurring on the IMP surface (i.e., oxygen reduction reaction) and leads to a rise in the local pH. Enhanced local alkalinity likely destabilizes the adjacent oxide layer faster, causing an apparent acceleration of trench propagation relative to EI conditions (Fig. 13a). This also potentially explains similarities in the optical microscopy images at the end of immersion in GC conditions (Fig. 4b, c) and previous observations of AA2024 corroding in elevated pH [51].

When streaking is present, a Mg- and Zn-rich surface layer dissolves rapidly [14,15], temporarily dominating the overall electrochemical response. The dissolution of this surface layer contributes to the galvanic current flowing to the AA2024 surface, as seen in the j_{gal} and E_{gal}

transients observed concurrently with streaking corrosion propagation (Fig. 14b, Fig. 15b). The presence of streaking corrosion leads to bursts of electron flow from AA7075 to AA2024. In our previous work, it was shown that streaking corrosion can temporarily inhibit dealloying of IMPs [15]. Interestingly, the trenching on the AA7075 side also appears to have been impacted by the streaking corrosion as it is less extensive (Fig. 4c, Fig. 7) than that seen in EI conditions. This suggests that the main anodic reaction on AA7075 potentially became the dissolution of the surface layer associated with streaking corrosion. As a result, the impact of microgalvanic coupling on the bulk matrix dissolution may have been reduced. The processes on the AA2024 side also appear to have been affected by extensive streaking. Specifically, the trench growth appeared to have been slowed down by the widespread surface layer dissolution, resulting in higher t_{fwt} values than trial 1. The slowdown may be due to the surface layer serving as a sacrificial anode for the AA2024 matrix. It is noted that the sizes of trenches on AA2024 side remained comparable to the EI conditions despite the slower growth which could be due to the resumption of trench propagation after streaking corrosion on the AA7075 side ended.

In Stage 3, corrosion behaviour is dominated by BT activity. For both alloys, the process underlying BT activity is potentially the dissolution of the oxide layer on the matrix surrounding the trenches due to the local pH generated on the IMP surface. This progresses at a more aggressive rate for AA2024 resulting in a more severe transformation. The local pH increase generated by IMP activity continues to rise, destabilizing the oxide layer and potentially creating conditions that are unfavourable for aluminium hydroxide precipitation [54]. This may explain the absence of visible corrosion products at the end of immersion. As trenching deepens, IMPs can also detach, exposing surrounding matrix areas to further attack due to copper redeposition from the IMPs. Despite also containing Cu-rich particles, AA7075 does not show a similar extent of copper redeposition or aggressive matrix attack as AA2024. One possible explanation is that Zn released during corrosion precipitates onto IMP surfaces (Fig. 7b) [40,41], passivating them and limiting cathodic reactions [40,41]. This helps suppress further degradation. The passivation of AA7075 IMPs might also explain why, at later stages of immersion, electrons generated by the dissolution of the AA7075 matrix flow to the AA2024 sites instead of being kept locally. The observed E_{gal} shift towards more positive values in trial 1 is consistent with copper redeposition. Meanwhile, the modest j_{gal} decrease in magnitude can be explained by the detachment of some IMPs in AA2024 or the reduction of AA7075 IMP activity due to Zn precipitation.

4. Conclusion

By combining in situ reflected light microscopy with galvanic current and potential measurements, this study revealed how galvanic coupling between AA2024 and AA7075 affects microscale local corrosion processes on both alloys. The results showed that such coupling drives electron flow from AA7075 to AA2024, increasing the cathodic activity of intermetallic particles in AA2024 and thereby intensifying local corrosion, despite the alloys' relatively small galvanic mismatch. The increased cathodic activity not only caused more extensive dissolution beyond the AA2024 IMP trenches, but also potentially increased the local pH near the AA2024 surface, which hindered corrosion product deposition. Galvanic coupling appeared to have minimal influence on the initial dealloying of IMPs in either alloy, though it modestly accelerated trench growth, with AA7075 trenches reaching full width in roughly half the time compared to electrically-isolated conditions. Streaking corrosion on AA7075 further modified the galvanic interaction, producing transients in the galvanic current and potential. Notably, extensive streaking corrosion coincided with reduced trenching on AA7075 and a temporary slowdown in trench widening on AA2024. Overall, this work highlights how macroscale galvanic coupling affects localised corrosion processes. It also shows the power of combining electrochemical techniques with site-resolved optical analysis to uncover mechanisms that would otherwise be overlooked or misidentified as typical local corrosion behaviour. At the same time, this integrated approach offers a pathway to link local corrosion dynamics with macroscale galvanic responses. Such insights may enable the use of galvanic measurements as practical indicators for tracking corrosion progression in real-life systems.

CRediT authorship contribution statement

Marlon Mopon: Writing – review & editing, Writing – original draft, Visualization, Methodology, Investigation, Formal analysis. **Arjan Mol:** Writing – review & editing, Writing – original draft, Formal analysis, Conceptualization. **Santiago J. Garcia:** Writing – review & editing, Writing – original draft, Visualization, Supervision, Methodology, Funding acquisition, Conceptualization.

Declaration of competing interest

The authors declare the following financial interests/personal relationships which may be considered as potential competing interests:

Marlon Mopon Jr. reports financial support was provided by DOST ERDT. If there are other authors, they declare that they have no known competing financial interests or personal relationships that could have appeared to influence the work reported in this paper.

Acknowledgements

The author acknowledges the financial support by the DOST ERDT Program and the Faculty of Aerospace Engineering at TU Delft.

Supplementary materials

Supplementary material associated with this article can be found, in the online version, at doi:10.1016/j.electacta.2025.147335.

Data availability

Data can be accessed in the 4TU repository through this link: doi:10.4121/59a35c61-d845–40ac-b0a7–975e70321006.

References

[1] L. Paussa, F. Andreatta, D. De Felicis, E. Bemporad, L. Fedrizzi, Investigation of AA2024-T3 surfaces modified by cerium compounds: a localized approach, Corros. Sci. 78 (2014) 215–222, https://doi.org/10.1016/j.corsci.2013.10.001.

[2] F.F. Chen, I. Cole, A.E. Hughes, A.M. Glenn, E. Sapper, J. Osborne, Microstructure characterisation and reconstruction of intermetallic particles, Mater. Corrosion 65 (2014) 664–669, https://doi.org/10.1002/maco.201307345.

[3] A.E. Hughes, R. Parvizi, M. Forsyth, Microstructure and corrosion of AA2024, Corros. Rev. 33 (2015) 1–30, https://doi.org/10.1515/corrrev-2014-0039.

[4] J.V. de Sousa Araujo, I. Costa, X. Zhou, Comparison of Constituent Intermetallic Particles in Different Aluminium Alloys, Metallogr. Microstruct. Anal. 14 (2025) 106–119, https://doi.org/10.1007/s13632-025-01170-w.

[5] A.S. Hammad, H. Lu, M.M. El-Sayed Seleman, R.Q. Dzakyprasetyo, A. Anawati, Corrosion Behaviour of Aluminum Alloy AA7075-T651, IOP. Conf. Ser. Mater. Sci. Eng. 541 (2019) 012006, https://doi.org/10.1088/1757-899X/541/1/012006.

[6] A. Kosari, H. Zandbergen, F. Tichelaar, P. Visser, P. Taheri, H. Terryn, J.M.C. Mol, In-situ nanoscopic observations of dealloying-driven local corrosion from surface initiation to in-depth propagation, Corros. Sci. 177 (2020) 108912, https://doi.org/10.1016/j.corsci.2020.108912.

[7] A. Kosari, F. Tichelaar, P. Visser, H. Zandbergen, H. Terryn, J.M.C. Mol, Dealloying-driven local corrosion by intermetallic constituent particles and dispersoids in aerospace aluminium alloys, Corros. Sci. 177 (2020) 108947, https://doi.org/10.1016/j.corsci.2020.108947.

[8] M. Olgiati, P.J. Denissen, S.J. Garcia, When all intermetallics dealloy in AA2024-T3: quantifying early stage intermetallic corrosion kinetics under immersion, Corros. Sci. (2021) 109836, https://doi.org/10.1016/j.corsci.2021.109836.

[9] T. Hashimoto, X. Zhang, X. Zhou, P. Skeldon, S.J. Haigh, G.E. Thompson, Investigation of dealloying of S phase (Al2CuMg) in AA 2024-T3 aluminium alloy using high resolution 2D and 3D electron imaging, Corros. Sci. 103 (2016) 157–164, https://doi.org/10.1016/j.corsci.2015.11.013.

[10] Y. Zhu, K. Sun, G.S. Frankel, Intermetallic Phases in Aluminum Alloys and Their Roles in Localized Corrosion, J. Electrochem. Soc. 165 (2018) C807–C820, https://doi.org/10.1149/2.0931811jes.

[11] N. Birbilis, M.K. Cavanaugh, R.G. Buchheit, Electrochemical behavior and localized corrosion associated with Al7Cu2Fe particles in aluminum alloy 7075-T651, Corros. Sci. 48 (2006) 4202–4215, https://doi.org/10.1016/j.corsci.2006.02.007.

[12] S. Niverty, C. Kale, K.N. Solanki, N. Chawla, Multiscale investigation of corrosion damage initiation and propagation in AA7075-T651 alloy using correlative microscopy, Corros. Sci. 185 (2021) 109429, https://doi.org/10.1016/j.corsci.2021.109429.

[13] S.S. Wang, J.T. Jiang, G.H. Fan, G.S. Frankel, L. Zhen, Effects of long-term natural aging on the altered surface layer on an Al-Zn-Mg-Cu alloy and on corrosion properties, Electrochim. Acta 266 (2018) 34–42, https://doi.org/10.1016/j.electacta.2018.02.001.

[14] Z. Zhao, G.S. Frankel, On the first breakdown in AA7075-T6, Corros. Sci. 49 (2007) 3064–3088, https://doi.org/10.1016/j.corsci.2007.02.001.

[15] M. Mopon, A. Mol, S.J. Garcia, Intermetallic particles trigger streaking corrosion in AA7075-T6, Npj. Mater. Degrad. 9 (2025) 92, https://doi.org/10.1038/s41529-025-00631-5.

[16] R.-S. Huang, C.-J. Lin, H.S. Isaacs, A Difference-Imaging Technique Used to Study Streaking Corrosion of Aluminum Alloys AA7075 and AA8006 in Chloride Solution, Electrochem. Solid-State Lett. 9 (2006) B11–B14, https://doi.org/10.1149/1.2140503.

[17] R.S. Huang, C.J. Lin, H.S. Isaacs, Measuring streaking rates of an Al–Zn alloy using a difference imaging technique, Corros. Sci. 48 (2006) 1867–1873, https://doi.org/10.1016/j.corsci.2006.05.039.

[18] U. Donatus, G.E. Thompson, X. Zhou, Effect of Near-Ambient Temperature Changes on the Galvanic Corrosion of an AA2024-T3 and Mild Steel Couple, J. Electrochem. Soc. 162 (2015) C42–C46, https://doi.org/10.1149/2.0551501jes.

[19] L. Shi, Y. Song, P. Zhao, H. Wang, K. Dong, D. Shan, E.H. Han, Variations of galvanic currents and corrosion forms of 2024/Q235/304 tri-metallic couple with multivariable cathode/anode area ratios: experiments and modeling, Electrochim. Acta 359 (2020) 136947, https://doi.org/10.1016/j.electacta.2020.136947.

[20] L. Shi, Y. Song, K. Dong, H. Wang, D. Shan, E.H. Han, The change of cathode/anode roles and corrosion forms in 2024/Q235/304 tri-metallic couple with the variation of oxygen concentrations and area ratios, Corros. Sci. 184 (2021) 109400, https://doi.org/10.1016/j.corsci.2021.109400.

[21] V. Torres, R. Mayen-Mondragon, J. Genesca, Assessment of the galvanic corrosion of bi-metallic couple 7075-T6-aluminum alloy/microalloyed dual-phase steel, Materials and Corrosion 73 (2022) 940–949, https://doi.org/10.1002/maco.202112934.

[22] R. Montoya, A.G. Ruiz-García, A. Ortiz-Ozuna, B. Ramírez-Barat, J. Genesca, Acidification of the electrolyte during the galvanic corrosion of AA7075: a numerical and experimental study, Materials and Corrosion 72 (2021) 1259–1269, https://doi.org/10.1002/maco.202012274.

[23] M. Montoya, J. Genesca, R. Montoya, The AA7075–CS1018 Galvanic Couple under Evaporating Droplets, Corrosion and Materials Degradation 5 (2024) 92–108, https://doi.org/10.3390/cmd5010005, 2024Vol. 5, Pages 92-108.

[24] R.S. Marshall, A. Goff, C. Sprinkle, A. Britos, R.G. Kelly, Estimating the Throwing Power of SS316 when Coupled with AA7075 Through Finite Element Modeling, Corrosion 76 (2020) 476–484, https://doi.org/10.5006/3438.

[25] Z. Feng, G.S. Frankel, C.A. Matzdorf, Quantification of Accelerated Corrosion Testing of Coated AA7075-T6, J. Electrochem. Soc. 161 (2014) C42–C49, https://doi.org/10.1149/2.059401jes.

[26] S. Niverty, N. Chawla, 4D microstructural characterization of corrosion and corrosion-fatigue in a Ti–6Al–4V /AA 7075-T651 joint in saltwater environment, Materials Science and Engineering: A 825 (2021) 141886, https://doi.org/10.1016/j.msea.2021.141886.

[27] S. Policastro, R. Anderson, C. Hangarter, D.J. Horton, J.A. Keith, M. C. Groenenboom, Galvanic Corrosion of AA7075-T6 Caused by Doped Titanium Oxides in a Controlled Atmospheric Environment, ECS. Trans. 80 (2017) 527–539, https://doi.org/10.1149/08010.0527ecst.

[28] L.B. Coelho, M. Hacha, Y. Paint, M.G. Olivier, Highlighting the effect of the aluminium alloy self-corrosion on the AA2024-T3/Ti6Al4V galvanic coupling in NaCl media, Surf. Interfaces. 16 (2019) 15–21, https://doi.org/10.1016/j.surfin.2019.04.004.

[29] D. Snihirova, D. Höche, S. Lamaka, Z. Mir, T. Hack, M.L. Zheludkevich, Galvanic corrosion of Ti6Al4V -AA2024 joints in aircraft environment: modelling and experimental validation, Corros. Sci. 157 (2019) 70–78, https://doi.org/10.1016/j.corsci.2019.04.036.

[30] S. Palani, T. Hack, J. Deconinck, H. Lohner, Validation of predictive model for galvanic corrosion under thin electrolyte layers: an application to aluminium 2024-CFRP material combination, Corros. Sci. 78 (2014) 89–100, https://doi.org/10.1016/j.corsci.2013.09.003.

[31] J.M. Vega, E. García-Lecina, J. Genesca, R. Montoya, The AA2024/CFRP galvanic couple under a dynamic electrolyte drop: modeling and experimental, Electrochim. Acta 432 (2022) 141137, https://doi.org/10.1016/j.electacta.2022.141137.

[32] N.M. André, A. Bouali, E. Maawad, P. Staron, J.F. dos Santos, M.L. Zheludkevich, S. T. Amancio-Filho, Corrosion behavior of metal–composite hybrid joints: influence of precipitation state and bonding zones, Corros. Sci. 158 (2019) 108075, https://doi.org/10.1016/j.corsci.2019.07.002.

[33] Z. Liu, M. Curioni, P. Jamshidi, A. Walker, P. Prengnell, G.E. Thompson, P. Skeldon, Electrochemical characteristics of a carbon fibre composite and the associated galvanic effects with aluminium alloys, Appl. Surf. Sci. 314 (2014) 233–240, https://doi.org/10.1016/j.apsusc.2014.06.072.

[34] M.M.Z. Ahmed, M.M. El-Sayed Seleman, D. Fydrych, G. Çam, Friction Stir Welding of Aluminum in the Aerospace Industry: the Current Progress and State-of-the-Art Review, Materials (Basel) 16 (2023) 2971, https://doi.org/10.3390/ma16082971, 2023Vol. 16, Page 2971.

[35] A. Murphy, W. McCune, D. Quinn, M. Price, The characterisation of friction stir welding process effects on stiffened panel buckling performance, Thin-Walled Structures 45 (2007) 339–351, https://doi.org/10.1016/j.tws.2007.02.007.

[36] C. Zhang, G. Huang, Y. Cao, Q. Li, Y. Zhu, X. Huang, Q. Liu, Investigation on microstructure and localized corrosion behavior in the stir zone of dissimilar friction-stir-welded AA2024/7075 joint, J. Mater. Sci. 55 (2020) 15005–15032, https://doi.org/10.1007/s10853-020-05072-w.

[37] S. Bocchi, M. Cabrini, G. D'Urso, C. Giardini, S. Lorenzi, T. Pastore, The influence of process parameters on mechanical properties and corrosion behavior of friction stir welded aluminum joints, J. Manuf. Process. 35 (2018) 1–15, https://doi.org/10.1016/j.jmapro.2018.07.012.

[38] A. Abdelfatah, M. Abu-Okail, L.Z. Mohamed, Corrosion behavior of the pre-heated friction stir welded AA2024 alloy reinforced with AA7075 in 3.5% NaCl solution, Int. J. Electrochem. Sci. 16 (2021) 151001, https://doi.org/10.20964/2021.01.44.

[39] C. Zhang, G. Huang, Q. Liu, Research on local corrosion behavior of thermo-mechanically affected zone in dissimilar AA2024/7075 friction stir welds, Intermetallics. (Barking) 130 (2021) 107081, https://doi.org/10.1016/j.intermet.2020.107081.

[40] A.F.S. Bugarin, C.P. De Abreu, M. Terada, H.G. De Melo, I. Costa, Effect of friction stir welding (FSW) on the electrochemical behavior and galvanic coupling of AA2024-T3 and AA7475-T651, Mater. Today Commun. 25 (2020) 101591, https://doi.org/10.1016/j.mtcomm.2020.101591.

[41] C.P. de Abreu, I. Costa, H.G. de Melo, N. Pébère, B. Tribollet, V. Vivier, Multiscale Electrochemical Study of Welded Al Alloys Joined by Friction Stir Welding, J. Electrochem. Soc. 164 (2017) C735–C746, https://doi.org/10.1149/2.0391713jes.

[42] L.B. Coelho, M. Taryba, M. Alves, M.F. Montemor, M.G. Olivier, Unveiling the effect of the electrodes area on the corrosion mechanism of a graphite - AA2024-T3 galvanic couple by localised electrochemistry, Electrochim. Acta 277 (2018) 9–19, https://doi.org/10.1016/j.electacta.2018.04.187.

[43] M. Mopon, A. Mol, S.J. Garcia, Effect of delayed inhibitor supply on AA2024-T3 intermetallic activity: a local in situ analysis with reflected microscopy, Corros. Sci. 230 (2024) 111910, https://doi.org/10.1016/j.corsci.2024.111910.

[44] M. Mopon, A. Mol, S.J. Garcia, Local re-immersion behaviour of Ce-based inhibiting layers on AA2024-T3 intermetallics: enhanced stability through partial dealloying and prolonged exposure, Corros. Sci. 255 (2025) 113146, https://doi.org/10.1016/j.corsci.2025.113146.

[45] M. Olgiati, P.J. Denissen, S.J. Garcia, When all intermetallics dealloy in AA2024-T3: quantifying early stage intermetallic corrosion kinetics under immersion, Corros. Sci. (2021) 109836, https://doi.org/10.1016/j.corsci.2021.109836.

[46] A. Boag, A.E. Hughes, A.M. Glenn, T.H. Muster, D. McCulloch, Corrosion of AA2024-T3 Part I: localised corrosion of isolated IM particles, Corros. Sci. 53 (2011) 17–26, https://doi.org/10.1016/j.corsci.2010.09.009.

[47] A. Kosari, M. Ahmadi, F. Tichelaar, P. Visser, Y. Gonzalez-Garcia, H. Zandbergen, H. Terryn, J.M.C. Mol, Editors' Choice—Dealloying-Driven Cerium Precipitation on Intermetallic Particles in Aerospace Aluminium Alloys, J. Electrochem. Soc. 168 (2021) 041505, https://doi.org/10.1149/1945-7111/abf50d.

[48] A.M. Homborg, M. Olgiati, P.J. Denissen, S.J. Garcia, An integral non-intrusive electrochemical and in-situ optical technique for the study of the effectiveness of corrosion inhibition, Electrochim. Acta 403 (2022) 139619, https://doi.org/10.1016/j.electacta.2021.139619.

[49] O. Gharbi, S. Kumar Kairy, P.R. De Lima, D. Jiang, J. Nicklaus, N. Birbilis, Microstructure and corrosion evolution of additively manufactured aluminium alloy AA7075 as a function of ageing, Npj. Mater. Degrad. 3 (2019) 40, https://doi.org/10.1038/s41529-019-0101-6.

[50] N. Birbilis, M.K. Cavanaugh, R.G. Buchheit, Electrochemical behavior and localized corrosion associated with Al7Cu2Fe particles in aluminum alloy 7075-T651, Corros. Sci. 48 (2006) 4202–4215, https://doi.org/10.1016/j.corsci.2006.02.007.

[51] E. Michailidou, P. Visser, J.M.C. Mol, A. Kosari, H. Terryn, K. Baert, Y. Gonzalez-Garcia, The effect of pH on the corrosion protection of aluminum alloys in lithium-carbonate-containing NaCl solutions, Corros. Sci. 210 (2023) 110851, https://doi.org/10.1016/j.corsci.2022.110851.

[52] C. Zhang, G. Huang, Y. Cao, Q. Li, Y. Zhu, X. Huang, Q. Liu, Investigation on microstructure and localized corrosion behavior in the stir zone of dissimilar friction-stir-welded AA2024/7075 joint, J. Mater. Sci. 55 (2020) 15005–15032, https://doi.org/10.1007/s10853-020-05072-w.

[53] P.J. Denissen, A.M. Homborg, S.J. Garcia, Interpreting Electrochemical Noise and Monitoring Local Corrosion by Means of Highly Resolved Spatiotemporal Real-Time Optics, J. Electrochem. Soc. 166 (2019) C3275–C3283, https://doi.org/10.1149/2.0341911jes.

[54] K.H. Gayer, L.C. Thompson, O.T. Zajicek, The solubility of aluminum hydroxide in acidic and basic medium at 25 °C, Can. J. Chem. 36 (9) (1958) 1268–1271, https://doi.org/10.1139/V58-184.